

行政院原子能委員會
委託研究計畫研究報告

SOFC 電池堆接合件高溫耐久機械性能分析

Analysis of High-Temperature Mechanical Durability of SOFC Stack Joints

計畫編號：1002001INER053

受委託機關（構）：國立中央大學

計畫主持人：林志光 教授

聯絡電話：03-4267340

E-mail address：t330014@cc.ncu.edu.tw

核研所聯絡人員：江烈光、劉建國、吳思翰

報告日期：100 年 11 月

目錄

頁數

中文摘要.....	1
英文摘要.....	2
1. INTRODUCTION	4
1.1 Solid Oxide Fuel Cell.....	4
1.2 Glass Sealant.....	5
1.3 Joint of Glass-Ceramic Sealant and Metallic Interconnect	7
1.4 Purposes and Scope.....	10
2. MATERIALS AND EXPERIMENTAL PROCEDURES	12
2.1 Mechanical Testing of Sintered GC-9 Glass.....	12
2.1.1 Materials and specimen preparation	12
2.1.2 Ring-on-ring test	13
2.1.3 Weibull statistic analysis.....	14
2.1.4 Microstructural analysis.....	15
2.2 Mechanical Testing of Joint of Glass-Ceramic Sealant and	
Metallic	15
2.2.1 Materials and Specimen Preparation	15
2.2.2 Mechanical testing	17
2.2.3 Microstructural analysis.....	17
3. RESULTS AND DISCUSSION.....	18
3.1 Sintered GC-9 Glass	18
3.1.1 Microstructure.....	18
3.1.2 Effect of environmental temperature on mechanical behavior..	19

3.1.3 Fracture strength and Weibull statistic analysis.....	21
3.1.4 Effect of environmental temperature on Young’s modulus	22
3.1.5 Failure analysis	22
3.2 Sintered GC-9 Glass	23
3.2.1 Effect of LSM coating on the joint strength.....	25
3.2.2 Creep rupture behavior	25
4. CONCLUSIONS	27
REFERENCES	29
TABLES	33
FIGURES	35

中文摘要

本研究主旨在探討經過不同時效處理之封裝玻璃陶瓷燒結試片，在不同測試溫度下 (25 °C-800 °C) 的機械強度與破壞模式，並評估含 $\text{La}_{0.67}\text{Sr}_{0.33}\text{MnO}_3$ (LSM) 塗層之金屬連接板與封裝玻璃陶瓷接合件於 800 °C 下之高溫機械強度。此外，也探討玻璃陶瓷和未含 LSM 塗層金屬連接板接合件於 800 °C 下的潛變性質。實驗結果顯示，經過 1000 小時時效處理後之玻璃陶瓷燒結試片，於 650 °C-750 °C 下之抗折強度比在 25 °C 高，此乃由於裂縫癒合效應所致，而於 800 °C 下的強度為最低。另外，無論測試溫度高低，經過 1000 小時時效處理之玻璃陶瓷試片強度優於 100 小時時效處理之試片，而未經時效處理之試片強度為三者最低，此乃時效時間越長，結晶化程度越高，玻璃陶瓷之強度也就越高。

有關玻璃陶瓷與含有 LSM 塗層之金屬連接板的高溫機械性質與破壞模式，結果顯示含有 LSM 塗層的接合件試片，其張力強度和剪力強度皆遠低於未含 LSM 塗層的接合件試片，此乃由於鉻酸鋇層產生微孔洞以及微裂縫所致。由微結構及破斷面分析結果發現含有 LSM 塗層的接合試片破壞皆發生於玻璃陶瓷基材與鉻酸鋇層的界面。未含 LSM 塗層之剪力試片破壞則發生於玻璃基材內部並伴隨鉻酸鋇層的剝落，而未含 LSM 塗層之張力試片破壞則發生於玻璃陶瓷基材內部。潛變接合件試片於 800 °C 下的潛變壽命會隨著負載減少而增加。在剪力試片方面，在 1000 小時壽命的潛變強度約為剪力接合件強度的五分之一，而張力試片在 1000 小時壽命的潛變強度則約為張力接合件強度的百分之八。另外，剪力試片在較短潛變壽命的破壞模式會與接合件強度測試的破壞模式相似，破壞皆發生在玻璃基材與鉻酸鋇層的界面，而較長潛變壽命試件的破壞則發生於玻璃基材內部並伴隨鉻酸鋇層的剝落，張力潛變試片破壞皆發生在玻璃基材與鉻酸鋇層的界面。

Abstract

Mechanical properties at various temperatures (25 °C-800 °C) were investigated for a newly developed solid oxide fuel cell glass sealant (GC-9) in variously aged conditions. The joint strength between the GC-9 glass-ceramic sealant and an interconnect steel (Crofer 22 H) coated with $\text{La}_{0.67}\text{Sr}_{0.33}\text{MnO}_3$ (LSM) was also investigated at 800 °C. In addition, creep rupture properties of the joint specimens were also investigated at 800 °C under constant loading. For the 1000 h-aged, sintered GC-9 glass, the flexural strength at 650 °C-750 °C was greater than that at 25 °C due to a crack healing effect. From the force-displacement curves of the 1000 h-aged GC-9 glass, the inferred glass transition temperature (T_g) was between 750 °C and 800 °C. Therefore, its flexural strength was significantly reduced at 800 °C due to a viscous effect. However, a greater flexural strength and stiffness of the aged GC-9 glass over the non-aged one was observed at temperature higher than 700 °C due to a greater extent of crystallization.

Both the shear and tensile bonding strength at 800 °C of the joint specimens coated with LSM were weaker than those of the non-coated ones. Through analysis of the interfacial microstructure, microvoids and microcracks were found at the BaCrO_4 chromate layer. When the LSM coating film and BaCrO_4 layer were joined together with incompatible deformation, microvoids/microcracks were formed at the BaCrO_4 layer. In this regard, the joint strength was degraded by such a coating. The creep rupture time of both shear and tensile joint specimens was increased with a decrease in the applied constant load at 800 °C. The creep strength at 1000 h under shear loading was about one fifth of the shear strength at 800 °C. The tensile creep strength at

1000 h was about 8% of the tensile strength at 800 °C. The failure pattern of the shear creep joint specimens with a shorter creep rupture time was similar to that of the shear joint strength test specimens while a different failure pattern was found for a longer creep rupture time.

1. INTRODUCTION

1.1 Solid Oxide Fuel Cell

Fuel cells have been well recognized as a clean, environment-friendly, effective and alternative energy converter for the conventional fossil fuels, which can convert chemical energy into electrical power through electrochemical reactions so that they. Among the fuel cells developed, solid oxide fuel cells (SOFCs) are the most efficient type. Compared with other fuel cells, the main features of the SOFC are that the utilization of solid oxides as the electrolyte which can prevent leakage or evaporation and the operating temperature is higher.

Figure 1 shows the operating principle of an SOFC using hydrogen as fuel [1]. The electrochemical reactions involved are shown below:



Oxidant flows through the cathode side such that oxygen is transformed into oxygen ions as a result of receiving electrons from the external circuit. By means of the thrust of differences in potential and concentration, oxygen ions migrate to the anode through oxygen vacancies in the electrolyte. Fuel such as hydrogen is fed into the anode side where it is oxidized by reacting with oxygen ions to produce water and release electrons to the external electrical circuit. The electrolyte conducts these ions between the electrodes by maintaining the overall electrical charge balance. Finally, the flow of electrons in the external circuit generates the electrical power, providing for electrical appliance.

SOFCs usually operate at 600-1000 °C because solid oxides possess sufficiently high ionic conductivity at elevated temperature. Without the noble catalysts, SOFCs can still proceed with electrochemical reactions. Through internal reforming, hydrocarbon fuels such as natural gas can be catalytically converted to hydrogen and carbon monoxide that can be directly used in SOFCs.

Tubular and planar cells are two typical configuration designs for SOFC developed. The planar type is expected to be cost effective and mechanically robust and offer high surface, volumetric and gravimetric power densities [2]. For a unit cell, it consists of anode, cathode and electrolyte to perform a

complete electrochemical reaction. In practical applications, a positive electrode-electrolyte-negative electrode (PEN) plate is fabricated by sintering anode, electrolyte and cathode together at high temperature. The power capacity of a single cell is limited. In order to obtain a higher voltage and power, interconnects which have high electrical conductivity and gas-separation ability are used to provide electrical conduction for several PEN plates in a serial connection. Structural scheme of a planar SOFC stack is shown in Fig. 2 [3]. Between an interconnect and PEN plate, a nickel mesh is inserted to work as both an electrical connector and fuel gas manifold. In addition, high-temperature hermetic sealants are needed and play an important role in planar SOFCs to seal SOFC components and prevent fuel and oxidant from mixing and leakage during operation.

1.2 Glass Sealant

Sealing designs developed for SOFC include rigid seals and compressive seals [4-6]. In the type of compressive sealing such as mica-based sealants, the major advantage is that these seals are not rigidly fixed to the other SOFC components. Therefore, these seals do not require very precise coefficient of thermal expansion (CTE) match. However, maintenance of gas-tight compressive sealing requires an application of constant load during operation. On the other hand, rigid seals, such as brazing, glass and glass-ceramic sealants, do not require such a mechanically applied pressure, but have more strict requirements for good adherence and CTE match to prevent leakage and cracking [4].

Glass sealants are used in planar SOFC stacks because of easy fabrication and usage. The glass transition temperature (T_g) is an important factor for selection of suitable glass sealants, because the key mechanism of the glass sealant at operating condition is viscosity [5]. Glass sealants are generally designed to soften and viscously flow to provide an adequate seal at operating condition by controlling the glass compositions to make the T_g lower than the operating temperature of SOFC.

The essential requirement for rigid sealing is that the CTE of the sealing material should closely match with other adjacent components such as the electrode and interconnect. Considerable stresses can be generated by temperature gradients and thermal expansion mismatch during thermal cycles. Glass sealants become brittle after melting and cooling such that they are very sensitive to cracking under tensile stresses [5]. Glass-ceramics are produced by

means of heat treatment to change the microstructure of glasses from an amorphous phase to crystalline phases, which can overcome the drawback of glasses. Therefore, glass ceramics have better mechanical properties and higher viscosity than glasses to withstand thermal stresses.

Many compositions of glass and glass-ceramic sealants for planar SOFC have been developed. According to a systematic classification on the basis of the primary glass-forming oxides, phosphate-based, borate-based and silicate-based glass-ceramics were sorted and reviewed in a few studies [4,5]. Due to volatilization and chemical interaction, applications of phosphate-based and borate-based glass-ceramics as sealants may cause negative effects on the SOFC stack [4,5]. Silicate-based glass-ceramics exhibit less interaction with other components, but greater CTE mismatch to other components [4]. For this reason, alkaline-earth oxides as modifiers were used to increase the CTE and improve the adhesion ability [4]. For example, BaO-CaO-Al₂O₃-SiO₂ (BCAS) glass systems have been developed for these purposes [2,7-15], with a focus on a commercial BCAS glass, designated as G-18 (35 mol% BaO, 35 mol% SiO₂, 15 mol% CaO, 10 mol% B₂O₃, and 5 mol% Al₂O₃).

Choi and Bansal [11] studied the mechanical properties of some glass sealants with different reinforcements. The flexure strength, fracture toughness, R-curve, hardness, elastic modulus, and density of the G-18 glass reinforced with 0, 10, 20, and 30 mol% of alumina platelets or 3 mol% YSZ particulates were determined at room temperature. Besides, the elevated-temperature constitutive relations of these materials were also investigated at 800 °C and 1000 °C. The strength and fracture toughness of the G-18 glass was improved with such reinforcements. The flexure strength, fracture toughness, hardness, and Young's modulus of the G-18 with alumina reinforcements were greater than those with YSZ. Addition of alumina did not have much effect on the density but addition of YSZ increased the density. In addition, the composite of G-18 with YSZ exhibited more intensively viscous behavior at both 800 °C and 1000 °C.

The hardness, Young's modulus, and creep properties of G-18 were also investigated using a nanoindentation technique [12]. To generate different degrees of crystallization, G-18 samples were sintered at 850 °C and aged at 750 °C for 5, 50, and 100 h. The tests were carried out at 25-400 °C. Results showed that the elastic modulus increased slightly with temperature. There was a significant jump of about 100% in the elastic modulus from 300 to 400 °C and the hardness had a similar trend. In addition, the samples having a higher degree of crystallization were more resistant to creep, and creep compliance

tended to decrease with an increase in testing temperature.

Mechanical properties of a newly developed GC-9 glass sealant at various temperatures are investigated by Chang [16]. The major contents of GC-9 glass include BaO, B₂O₃, Al₂O₃, and SiO₂. GC-9 samples were sintered at 850 °C and aged at 750 °C for 4 and 100 h, designated as non-aged and aged sintered GC-9 glass, respectively, for generating different degrees of crystallization [16]. Results showed that the extent of crystallization was increased with a longer aging time, but the types of crystalline phases were not changed [16]. At temperature below the glass transition temperature (T_g), both the non-aged and aged, sintered GC-9 glass had a significant strength improvement due to a crack healing effect [16]. In addition, a greater flexural strength and stiffness of the aged, sintered GC-9 glass over the non-aged one was observed at temperature higher than 700 °C due to a greater extent of crystallization [16]. However, with a longer aging time, the sintered GC-9 glass had a greater flexural strength and stiffness, but the ability for relaxing thermal stresses at high temperature may be decreased due to a less amount of residual glass [16].

1.3 Joint of Glass-Ceramic Sealant and Metallic Interconnect

Joining glass ceramic sealants with metallic interconnects is very common when a rigid type of sealing is applied to intermediate-temperature planar SOFC (IT-pSOFC). Figure 3 [5] shows the locations where seals are used in a planar SOFC stack with metallic internal gas manifolds and metallic interconnects. Common seals include: (a) cell to metal frame; (b) metal frame to metal interconnect; (c) frame/interconnect pair to electrically insulating spacer; (d) stack to base manifold plate [5]. Seals (b) and (d) can be referred to as a joint of glass-ceramic sealant and metallic interconnect.

Generation of thermal stresses cannot be avoided during cyclic operation of SOFC leading the seals to be subjected to tensile and shear stresses [17-19]. The seals may fail resulting in degradation of cell performance if the stresses exceed the corresponding strength of the joint. For this reason, it is necessary to investigate the mechanical properties of the joint of glass-ceramic sealant and metallic interconnect for assessment of the structural reliability of an SOFC stack. The mechanical properties of a joint do not belong to that of a single material while they are interfacial properties between two materials. Any interaction between glass ceramic and metal may influence the mechanical properties of the joint. Unfortunately, these interactions such as undesirable chromate formation [14] and electrical short-circuiting [7] are difficult to avoid

if ferritic chromia-forming alloys are applied as the interconnect. There is little work in the literature related to the mechanical properties of such a joint in SOFC. A few studies [2,6,10,14,15,20-22] have investigated this subject which is important to advance the development of SOFC technologies.

Various testing techniques have been applied to characterize the joint strength between glass ceramic sealants and metallic interconnects in SOFC. A modified rupture testing technique was developed by placing a sealed disk specimen in a test fixture and pressurizing the backside of the sample until rupture of seal [10]. In that study, an anode-supported bilayer (NiO-5YSZ/5YSZ) and eight different ferritic stainless steels, five of which had a chromia scale and three of which had an alumina scale, were sealed using a G-18 paste to make sealed disk specimens. In addition to testing as-joined specimens, aging tests were conducted by exposing the sealed disk specimens to ambient air at 750 °C for various hold times. Cyclic thermal testing was performed between room temperature and 750 °C for a number of cycles. It was found that alumina-forming ferritic steel substrates offered greater bond strength with G-18 in both the as-joined and exposure tested conditions [10]. The composition and thickness of the reaction zone between the metal's oxide scale and G-18 glass were the dominant factors in determining the joint strength [10]. The barium chromate layer that developed on the chromia-forming steels exhibited poorer thermal expansion match and tended to grow to a greater thickness than the celsian zone observed on the alumina-formers [10].

Smeacetto et al. [20] evaluated the tensile joint strength between a glass ceramic ($\text{SiO}_2\text{-Al}_2\text{O}_3\text{-CaO-Na}_2\text{O}$, SACN) and a metallic interconnect (Crofer 22 APU) at room temperature. Examination of the fractured samples revealed that fracture always occurred in the glass ceramic and never at the interface of the joint [20]. The interfacial strength between the G18 glass ceramic and Crofer 22 APU substrate was tested at temperatures ranging from 25 to 800 °C under both tensile and shear loading in another study by Stephens et al. [15]. However, two different failure modes were observed in the tensile tests: glass bulk failure mode referring to failure occurring through the glass layer, and interfacial failure mode referring to failure occurring at the glass-metal interface [15]. In the study of Malzbender et al. [2], a symmetric shear test was developed to characterize the shear strength of the joint between a glass-ceramic sealant ($\text{BaO-CaO-Al}_2\text{O}_3\text{-SiO}_2$, BCAS) and a Crofer 22 APU interconnect at the SOFC operating temperature. In addition to shear strength, shear modulus and viscosity of the joint were also determined by a rheological model [2]. At the SOFC operating temperature, the as-joined specimens exhibited viscous shear

deformation while the viscous shear deformation became more difficult for additionally crystallized specimens [2].

The tensile joint strength of a novel high-temperature sealing glass ($\text{SrO-CaO-Y}_2\text{O}_3\text{-B}_2\text{O}_3\text{-SiO}_2$) with a metallic interconnect (Crofer 22 APU) at room temperature was investigated by Chou et al. [14]. The bonding/wetting behavior of glasses to metals is intensely dependent on the nature of the surface of the metal. The samples were pre-oxidized to generate oxide layers to simulate long-term exposure conditions. Effects of environmental aging, including oxidizing and reducing, were also studied. In a further study of Chou et al. [21], effect of aluminization of the metallic interconnect on the tensile strength of the joint at room temperature was studied. Three different processes for aluminization were evaluated. The results of that study [21] showed that aluminization could reduce undesirable chromate formation between alkaline earth silicate sealing glass and chromia-forming alloys.

In order to make a good adhesion between an AISI 430 steel and a glass-ceramic sealant, a pre-oxidation heat treatment was essential, as described in Ref. [20]. For the case of as-received AISI 430 without pre-oxidation treatment, the glass-ceramic sealant was more easily detached from the metallic interconnect. In the study of Donald [6], an appropriate metal oxide layer was generated by pre-oxidization of a metal substrate before sealing process. During sealing process, the oxide layer dissolved into the glass, and the interface between the glass and metal became saturated such that favorable bonding conditions would then prevail over the interface [6]. However, if sealing is attempted to a clean metal surface, a suitable redox reaction between the glass and metal is needed to achieve conditions suitable for chemical bonding [6]. It indicates that a pre-oxidization layer can provide the favorable bonding conditions with no need of a suitable redox reaction before the sealing process. A new glass was designed and used to join YSZ to Crofer 22 APU in a study by Smeacetto et al. [22]. Aging treatment in air caused a Cr-diffusion from Crofer 22 APU alloy to the glass-ceramic sealant only when the alloy was in the as-received condition, whereas the pre-oxidized specimens did not exhibit migration of Cr through the glass-ceramic sealant.

During SOFC operation, vaporization of Cr-rich species from interconnect materials is a major source of degradation that limits the lifetime of planar SOFC systems with metallic interconnects. In order to solve this problem, a few studies [23-26] applied $\text{La}_{0.67}\text{Sr}_{0.33}\text{MnO}_3$ (LSM) coating on metallic interconnects to prevent Cr poisoning of the planar SOFC. However, the influence of LSM coating on the joining strength between the metallic connect

and glass-ceramic sealant was not investigated in those studies [23-26]. It is necessary to investigate the influence of LSM coating on the joining strength between the metallic connect and glass-ceramic sealant.

1.4 Purpose and Scope

Glasses and glass ceramics are currently the most popular candidates for planar SOFC sealants. It is difficult to repair or replace such sealants because they are bonded to several components. Therefore, glass and glass-ceramic sealants must have stable properties and long-term durability. A new glass sealant (designated as GC-9) of the BaO-B₂O₃-Al₂O₃-SiO₂ system for use in IT-pSOFC at 700-750 °C has recently been developed at the Institute of Nuclear Energy Research (INER). This new glass sealant is a silicate-based glass and one of the promising glasses to be used for IT-pSOFC. The viscosity, CTE, and crystallization of this sealant, and the chemical interaction between this sealant and other planar SOFC components (electrolyte, electrode, interconnect, and frame) have been investigated [27-29]. As reported in those studies, this new glass showed good chemical and thermal compatibility with other components and is to be used in a prototypical planar SOFC stack being developed at INER. Therefore, it is important and necessary to study the high-temperature mechanical properties of this newly developed glass sealant so as to assess the structural integrity of a planar SOFC stack during cyclic operation.

The high operating temperature enables SOFCs to obtain a superior efficiency of energy conversion while accompanying concerns such as degradation of materials due to undesirable reactions between components. Structural durability of SOFC is affected by the thermal stress caused by considerable CTE mismatch between components and thermal gradient. Excessive thermal stresses may lead to fracture of components endangering the mechanical integrity of an SOFC stack. Therefore, a systematic investigation of mechanical properties of joints between the glass-ceramic sealant and metallic interconnect at room temperature and operating temperature is essential for development of a reliable SOFC stack.

There are two main objectives in the present study. Firstly, mechanical properties at various temperatures were investigated for the newly developed GC-9 glass sealant in sintered powder forms. Variation of the elastic modulus and mechanical strength with temperature for this glass was studied by conducting ring-on-ring tests at room temperature to 800 °C. As the glass

applied to planar SOFC stack may crystallize during assembling process and operation at high temperature, the effect of crystallization on mechanical properties of GC-9 was characterized. Secondly, mechanical properties of the joint between the GC-9 glass-ceramic sealant and an interconnect steel were also investigated. Two loading modes, tensile and shear loading, were applied to characterize the mechanical properties of the joint at both room temperature and 800 °C. Effects of $\text{La}_{0.67}\text{Sr}_{0.33}\text{MnO}_3$ (LSM) coating on the bonding strength of the joint were evaluated. In addition, creep properties of the GC-9 glass alone and its joint with an interconnect steel at 800 °C were also investigated. Microstructural and fractography analyses were conducted with scanning electron microscopy (SEM) and correlated with the mechanical testing results. It is hoped that results of the current study can provide some useful information for assessing the long-term structural reliability of planar SOFC.

2. MATERIALS AND EXPERIMENTAL PROCEDURES

2.1 Mechanical Testing of Sintered GC-9 Glass

2.1.1 Materials and specimen preparation

In the present work, the given GC-9 glass sealant was developed at INER for use in IT-pSOFC. The major composition of the GC-9 glass sealant includes 0-40 mol% BaO, 0-40 mol% SiO₂, 0-15 mol% B₂O₃, 0-15 mol% CaO, 0-15 mol% La₂O₃, 0-10 mol% Al₂O₃, and 0-5 mol% ZrO₂. It was made by mixing the constituent oxide powders and then melting at 1550 °C for 10 h. After melting, it was poured into a mold preheated to 680 °C to produce GC-9 glass ingots. The GC-9 glass ingots were then annealed at 680 °C for 8 h and cooled down to room temperature.

GC-9 glass powders were made by crushing the as-cast glass ingots and sieving with 325 mesh sieves. The average size of the glass powder is 45 μm. Slurries were made by adding into the GC-9 powders the desired amounts of solvent (alcohol), binder (ethyl celluloid), and plasticizer (polyethylene glycol). The slurries were dried at 80 °C for 1 h and the mixture was ground into powders again after well mixing. The GC-9 glass powders were then put into a mold and pressed to form a circular disk with a diameter of 40 mm and thickness of 1.5 mm for ring-on-ring test. A set of circular disk-shape specimens were heat-treated in air by the following steps: heated from room temperature to 550 °C at 5 °Cmin⁻¹, held at 550 °C for 1 h, heated up to 850 °C at 5 °Cmin⁻¹, sintered at 850 °C for 4h, cooled down to 750 °C at 5 °Cmin⁻¹, held at 750 °C for 1000 h, and cooled down to room temperature. Specimens through such heat-treatments are designated as 1000 h-aged, sintered GC-9 glass. In order to understand the effects of crystallization under a longer aging time on the mechanical properties of the sintered GC-9 glass, mechanical testing results of these 1000 h-aged specimens were made a comparison with those of shorter aging time in a previous study [16]. Flexural strength of similar specimens with an aging time of 4 h or 100 h at 750 °C have been tested [16], and they are designated as non-aged and 100 h-aged, sintered GC-9 glass. Another set of 100 h-aged specimens were made in the current study for creep testing. All of the specimens were polished with an 80-grit SiC paper to reduce surface roughness before mechanical testing. The thermal properties, such as T_g, softening temperature (T_s), crystallization temperature (T_c), and CTE, were determined by differential scanning calorimetry (DSC) and thermomechanical

analysis (TMA) at INER [27-29]. Figure 4 shows the DSC curve of the GC-9 glass [27]. The thermal expansion data for the non-aged bulk GC-9 glass, non-aged, sintered GC-9 glass, a positive electrode-electrolyte-negative electrode (PEN) assembly, and Crofer 22 APU steel are shown in Fig. 5 [29]. The T_g , T_s , T_{c1} , and T_{c2} of the bulk GC-9 glass are 668 °C, 745 °C, 820 °C, and 864 °C, respectively.

2.1.2 Ring-on-ring test

Because edge effects can be minimized, biaxial flexural test is a suitable method for determining of the strength of plate-like materials. In the current work, a biaxial flexural ring-on-ring test of the ASTM Standard C1499 [30] was applied to determine the mechanical properties of the 1000 h-aged, sintered GC-9 specimens at different testing temperatures. The ring-on-ring tests were performed using a commercial closed-loop servo-hydraulic material test machine attached with a furnace. The flexural loading fixture with a 10-mm-diameter inner loading ring and 20-mm-diameter outer supporting ring was made of alumina in order to perform tests at high temperatures. Schematic of the ring-on-ring test fixture is shown in Fig. 6. The testing temperatures were set at 25 °C, 650 °C, 700 °C, 750 °C, and 800 °C. For each high-temperature test, the specimen was heated to the specified temperature at a heating rate of 6 °Cmin⁻¹. The specimen was then held at the specified temperature for 3 min before applying the load. The load was applied under displacement control with a displacement rate of 0.0005 mms⁻¹ for all the given testing temperatures. The load-displacement relationship was recorded for each test to calculate the flexural strength and other properties. In addition, creep test of the 100 h-aged, sintered GC-9 glass was conducted under constant load at 800°C. Four load levels were selected to perform the creep test and get the stress-rupture time relationship. For each applied constant load, 4-5 specimens were used for repeated creep tests. After ring-on-ring tests, fracture surfaces of the broken specimens were observed with SEM to identify the fracture origins and mechanisms.

According to ASTM Standard C1499 [30], the formula for the biaxial flexural strength, σ_f , of a circular plate is given as

$$\sigma_f = \frac{3P}{2\pi h^2} \left[(1-\nu) \frac{D_s^2 - D_L^2}{2D^2} + (1+\nu) \ln \frac{D_s}{D_L} \right] \quad (4)$$

where P is the maximum applied force, h is the thickness of specimen, and D_L , D_S , and D are the diameters of the load ring, support ring and specimen, respectively. In the present study, the Poisson's ratio ν in Eq. (4) was assumed equal to 0.3. The deflection contour in the thickness direction from center to edge of the specimen was derived from a previous study [31] and is given as

$$\delta = \frac{3P(1-\nu^2)R_L^2}{2\pi h^3 E} \left\{ \left(\frac{R_S}{R_L} \right)^2 - 1 - \left[\left(\frac{R}{R_L} \right)^2 + 1 \right] \ln \left(\frac{R_S}{R_L} \right) + \frac{1}{2} \frac{1-\nu}{1+\nu} \frac{R_S^2 - R_L^2}{R_{SP}^2} \frac{R_S^2 - R^2}{R_L^2} \right\} \text{ for } 0 \leq R \leq R_L \quad (5)$$

where δ is the deflection of the specimen, R is the radial distance from the disk center to specified point, and R_L , R_S , R_{SP} are the radii of the load ring, support ring, and specimen respectively. Rearrangement of Eq. (5) and the Young's modulus of the sintered GC-9 glass can be calculated through the following formula

$$E = \frac{3P(1-\nu^2)R_L^2}{2\pi h^3 \delta} \left\{ \left(\frac{R_S}{R_L} \right)^2 - 1 - \left[\left(\frac{R}{R_L} \right)^2 + 1 \right] \ln \left(\frac{R_S}{R_L} \right) + \frac{1}{2} \frac{1-\nu}{1+\nu} \frac{R_S^2 - R_L^2}{R_{SP}^2} \frac{R_S^2 - R^2}{R_L^2} \right\} \quad (6)$$

The term $P\delta^{-1}$ can be determined from the slope of the force-displacement curve recorded in the ring-on-ring test.

2.1.3 Weibull statistic analysis

The Weibull statistics [32] is widely applied to describe the fracture behavior of brittle materials. Based on a weakest-link hypothesis, it is assumed that the most severe flaw controls the strength. When subjected to an applied stress, σ , the cumulative probability of failure for a brittle material can be expressed by [32]

$$F = 1 - \exp \left[- \left(\frac{\sigma - \sigma_u}{\sigma_o} \right)^m \right] \quad (7)$$

where F is the failure probability for an applied stress σ , σ_o is the Weibull characteristic strength (which corresponds to $F = 63.2\%$, or a value of zero for $\ln \ln(1/(1-F))$), σ_u is the threshold stress (below which no failure will occur), and m is the Weibull modulus. Here, the Weibull modulus m is a measure of the degree of strength data dispersion. If σ_u is assumed to be zero, Eq. (7)

becomes a two-parameter relation, as shown below [32]

$$F = 1 - \exp \left[- \left(\frac{\sigma}{\sigma_o} \right)^m \right] \quad (8)$$

This two-parameter Weibull probabilistic equation was applied to analyze the scattering and reliability of the flexural strength data generated in the current study. In order to have enough data points for Weibull analysis, more than fifteen specimens were repeatedly tested at each given testing condition.

2.1.4 Microstructural analysis

After mechanical testing, crystalline phases of the 1000 h-aged, sintered GC-9 glass were determined by X-ray diffraction (XRD) and SEM was applied to analyze the microstructure and crystalline morphology. The results of microstructural analysis were compared with those of the non-aged and 100 h-aged, sintered GC-9 glass in a previous study [16].

2.2 Mechanical Testing of Joint of Glass-Ceramic Sealant and Metallic Interconnect

2.2.1 Materials and specimen preparation

As mentioned in Section 1.3, glass-ceramic sealants are applied to bond each layer together and prevent leakage of air and fuel for a planar SOFC stack. Among the four sealing locations shown in Fig. 3, sealants used to seal a metallic frame to a metallic interconnect (S2) and a stack to a base manifold plate (S4) are classified as a joint of glass-ceramic sealant and metallic interconnect. In order to simulate the conditions of a joint subjected to thermal stresses at room temperature and operating temperature, two types of sandwich-like specimens (metal/sealant/metal) were designed in this study for determining the mechanical properties of the joint and investigating the interfacial reactions.

The metallic parts of the joint specimens were made of a commercial ferritic stainless steels, Crofer 22 H (ThyssenKrupp VDM GmbH, Werdohl, Germany), which is a heat-resistant alloy developed for application in SOFCs. Chemical compositions of the alloy are listed in Table 1. Table 2 [33] shows the

mechanical properties of Crofer 22 H alloy. For Crofer 22 H, the yield strength, ultimate tensile strength, and Young's modulus were decreased but the elongation was increased with an increase in temperature. The aforementioned GC-9 glass ceramic was used to join the two metal slices to make the sandwich specimens. Table 3 shows the Weibull characteristic strength and Weibull modulus of the sintered GC-9 glass at various temperatures.

Figure 7 shows the scheme of two types of joint specimens for tensile test (Fig. 7(a)) and shear test (Fig. 7(b)), respectively. The as-received, 2.5 mm-thick metal plates were cut into rectangular slices with dimensions of 95 mm x 25 mm x 2.5 mm. A pin hole was drilled in each steel slice for applying pin loading. In order to minimize bending and twisting effects during test, the force was applied by means of pin loading. For shear specimens, one edge of each steel slice was milled from the original thickness of 2.5 mm to 1 mm with an area of 8 mm x 25 mm. After machining, a GC-9 glass slurry was spread on the joining region of each steel slice to make a half-specimen. The nominal joining areas were 25 mm x 2.5 mm and 25 mm x 6 mm for tensile and shear specimens, respectively. The glass slurry was made of a mixture of GC-9 glass powders dispersed in ethanol. The half-specimen was then put in a furnace to dry the slurry at 70 °C. A joint specimen was assembled by placing a half-specimen onto another one to form a steel/glass ceramic sealant/steel sandwich specimen through appropriate heat treatments. In the assembling procedures, the joint specimens were firstly held at 500 °C for 1 h and heated to 900 °C with a hold time of 4 h. The heating rate at each heating step in the given assembling processes is 5 °C/min.

To investigate the influence of $\text{La}_{0.67}\text{Sr}_{0.33}\text{MnO}_3$ (LSM) coating on the joining strength of joint specimens, some of the metallic slices were coated with LSM before spreading the GC-9 glass slurry. In the current study, the joint specimens with LSM coating and without LSM coating are designated as CHT900 and HT900, respectively. The LSM films were deposited by pulsed direct current magnetron sputtering in a turbo-pumped vacuum chamber. The thickness of LSM film deposited on the Crofer 22 H slice was about 1.5 to 2 μm , followed by spreading the GC-9 glass slurry. The assembling process of the joint specimens with LSM coating is the same as that described in the previous section.

2.2.2 Mechanical testing

The HT900 and CHT900 joint specimens were tested under uni-axial

loading on a commercial closed-loop servo-hydraulic test machine (MTS 810) attached with a furnace. For high-temperature tests, the specimens were heated to 800 °C with a rate of 5 °C/min and held for 15 min to reach thermal equilibrium before applying the load. The mechanical tests were conducted by means of displacement control with a loading rate of 0.5 mm/min to determine joint strength. For each case, about 5-7 specimens were repeatedly tested and the average strength was determined. Besides, creep tests of the HT900 joint specimens were also conducted at 800 °C under constant loading using a direct-load creep test machine. Four constant load levels were selected to perform the creep tests based on the strength data of Chen [34]. About 5 specimens were repeatedly tested at each constant load level.

2.2.3 Microstructural analysis

After mechanical testing, fracture surface of each specimen was examined with an optical microscope to determine the true joining area. In order to investigate the characteristics of interfaces in the joint, some samples were cut along the longitudinal direction to observe the cross section of the joint. The cross sections of the samples were finely polished to optical finish. SEM was also adopted to examine the interfacial morphology between the glass-ceramic sealant and metallic interconnect. An energy dispersive spectrometer (EDS) module was used for composition analysis in order to determine the elemental distribution in the glass-ceramic sealant and metallic interconnect. The fracture mode of the joint under tensile stress and shear stress were also characterized.

3. RESULTS AND DISCUSSION

During operation cycles, glass-ceramic sealants suffer thermal stresses in tensile and shear modes due to CTE mismatch between glass-ceramic sealants and other components in a planar SOFC stack [17]. Unfortunately, the thermal stresses caused by CTE mismatch are inevitable because the glass-ceramic sealants are rigidly bonded with adjacent components. If the thermal stresses reach certain critical values, the glass-ceramic sealants may fail due to fracture of bulk material or interfacial delamination between the joining surfaces. In order to avoid these problems, there are two approaches: (a) improvement of the mechanical properties of glass-ceramic sealants; (b) enhancement of interfacial bonding strength between the glass-ceramic sealants and metallic interconnects. Formation of adhesive oxide layers is the main mechanism of interfacial joining between the glass ceramic and metallic interconnect. The bonding strength of the joint originates from the mutual Van Der Waals force of the formed oxide layers. The high-temperature joining mechanism of the GC-9 glass ceramic and Crofer 22 H alloy involves formation of two oxide layers with a Cr_2O_3 layer on the surface of Crofer 22 H connected with a BaCrO_4 layer on the surface of GC-9 [34].

In the following discussion, some of the results have been reported in the theses of Chang [16] and Chen [34], who worked together with the author on the current subject. The current work is an extension study of the previous work of Chang [16] and Chen [34], as more specimens were tested to get more data for a comprehensive study of the investigated issues.

3.1 Sintered GC-9 Glass

3.1.1 Microstructure

Crystalline phases of the sintered GC-9 glass were characterized by XRD. Figure 8 shows the XRD patterns of the 1000 h-aged, sintered GC-9 glass in comparison with the non-aged and 100 h-aged ones [16]. As shown in Fig. 8, there are several phase peaks present in the curves of the non-aged, 100 h-aged, and 1000 h-aged GC-9 glass indicating existence of certain crystalline phases in these materials. The main phase peaks in the XRD pattern of the non-aged and 100 h-aged GC-9 glass correspond to structures of BaSiO_3 , $\alpha\text{-Ba}(\text{Al}_2\text{Si}_2\text{O}_8)$, and $\text{Ba}_3\text{La}_6(\text{SiO}_4)_6$. On the other hand, crystallization also took place in the

1000 h-aged GC-9 glass and the dominant crystalline phases are $\text{Ca}(\text{Al}_2\text{Si}_2\text{O}_8)$ and $\alpha\text{-Ba}(\text{Al}_2\text{Si}_2\text{O}_8)$ in addition to Al_2SiO_5 . Therefore, a longer aging time generated additional crystalline phases in the sintered GC-9 glass.

Microstructure of the non-aged, and 100 h-aged GC-9 is shown in Fig. 9 [16]. There are some needle-shape crystals and aggregated particles observed in both conditions. The major crystalline phase is $\alpha\text{-Ba}(\text{Al}_2\text{Si}_2\text{O}_8)$ with a needle-shape form. Because the aggregated particles were buried in the residual glass of sintered GC-9 glass, it is hard to identify their phases. Throughout the non-aged and 100 h-aged GC-9 glass body were found microvoids resulting from burning of the binder or plasticizer during sintering process. The primary crystallization of the sintered GC-9 glass took place at the surfaces of glass powders as well as nucleating agents. The non-aged GC-9 glass exhibited pores (Fig. 9(a)), but pores in the 100 h-aged one had a different morphology (Fig. 9(c)) after heat treatment [16]. In addition, re-crystalline phases were occasionally found on the original crystalline phases, as shown in Fig. 9(e) [16]. In comparison with the non-aged GC-9 glass, though types of crystalline phase after aging at 750 °C for 100 h were not changed in the sintered GC-9 glass, microvoids between needle-shape crystals and aggregated particles might be filled with residual glass or re-crystalline phases due to a longer aging time. The re-crystalline phases in the 100 h-aged GC-9 glass were present at some areas but not everywhere. Fig. 10 shows the microstructure of the 100 h-aged specimen in which no re-crystalline phases were found. In comparison with Fig. 9(d), the re-crystalline phases were not visible in Fig. 10(b). For this reason, re-crystalline phases were not distributed evenly in the 100 h-aged GC-9 glass. Figure 11 show the microstructure of the 1000 h-aged GC-9 glass. Needle-shape crystals and aggregated particles are clearly observed as those in the previous two conditions. In comparison with the 100 h-aged GC-9 glass (Fig. 10), needle-shape crystals became coarser in the 1000 h-aged one due to a longer aging time. There are also some re-crystalline phases observed in the 1000 h-aged GC-9 glass, as shown in Figs. 11(b) and (c).

3.1.2 Effect of environmental temperature on mechanical behavior

Figure 12 shows the typical force-displacement curves of the non-aged, 100 h-aged, and 1000 h-aged, sintered GC-9 glass under a displacement rate of 0.0005 mms^{-1} at 25 °C, 650 °C, 700 °C, 750 °C, and 800 °C. Note that data of the non-aged and 100 h-aged conditions are taken from Ref. [16]. Although

some specimens did not break into pieces at 750 °C or 800 °C for the non-aged GC-9 glass, cracks were still formed on the tensile surfaces of these specimens. Such specimens were considered fractured as cracks were formed. For the non-aged GC-9 glass tested at 700 °C and below, the force-displacement relationship remained almost linear until final fracture, while those at 750 °C and 800 °C were non-linear (Fig. 12(a)) [16]. However, the 100 h-aged and 1000 h-aged GC-9 glass exhibited more brittleness, as they showed a brittle fracture pattern at temperature up to 750 °C. For the non-aged GC-9 glass, brittle fracture was observed at temperature 700 °C and below, and stress relaxation occurred at 750 °C and 800 °C. For the non-aged specimens tested at 750 °C and 800 °C, cracks were formed on the tensile surface at the first drop of force in the force-displacement curve. After this force drop, the surface cracks continued to grow as the bi-axial ring-on-ring test went on. At the same time, stress relaxation also took place during the test under a constant displacement rate of 0.0005 mms⁻¹. Because of such a stress-relaxation mechanism, the cracked specimens were not broken when the test was terminated. The stress relaxation mechanism in the non-aged GC-9 glass may involve viscoelastic behavior of porous and glassy phases, crystallite/glass phase decohesion, microcracking and/or plasticity of the residual glassy phases [35].

In Fig. 12(c), the trends of the force-displacement curves of 1000 h-aged GC-9 glass are similar to those of 100 h-aged one (Fig. 12(b)) [16]. For both 100 h-aged and 1000 h-aged GC-9 glass, there was no stress relaxation at 750 °C, but there was a serration in the force-displacement curve at 800 °C. Such a serrated force-displacement curve indicates that some surface cracks were formed at the first drop of force. Growth of these cracks was retarded by crystalline phases so that the applied force needed to be increased again to overcome these barriers. This phenomenon repeated several times and the specimen did not break into pieces until the test was terminated. As described above, degree of crystallization, re-crystallization, and pores filled with the residual glass and re-crystalline phases might influence the mechanical properties at high temperatures. With an increasing extent of crystallization, a less amount of residual glass could release the stress at high temperature so that there was no obvious relaxation phenomenon for the 100 h-aged and 1000 h-aged GC-9 glass at 750 °C and 800 °C.

3.1.3 Fracture strength and Weibull statistic analysis

The two-parameter Weibull distribution (Eq. (8)) of flexural strength for the 1000 h-aged, sintered GC-9 glass at different temperatures is shown in Fig. 13. Table 3 lists the Weibull characteristic strength, σ_0 , and Weibull modulus, m , for the non-aged, 100 h-aged, and 1000 h-aged, sintered GC-9 glass at various temperatures. The average flexural strength for variously aged GC-9 glass at different temperatures is given in Table 4. As shown in Fig. 13 and Table 3, the 1000 h-aged GC-9 glass exhibited a greater strength at 650 °C, 700 °C, and 750 °C than that at room temperature due to a crack healing effect, which is similar to the 100 h-aged one. The data points at these three testing temperatures are almost merged together in Fig. 13. Comparisons of the flexural strength of the given three aged conditions at each testing temperature are shown in Fig. 14 and Table 3. Note that the flexural strength of the 1000 h-aged and 100 h-aged GC-9 glass at 750 °C and 800 °C was about twice that of the non-aged one. As shown in Fig. 14, the 1000 h-aged condition always has the greatest flexural strength at each testing temperature. This can be attributed to a greater extent of crystallization due to a longer aging time. Generally, crystalline phases in the glass and glass ceramic can enhance mechanical strength. The 100 h-aged and 1000 h-aged GC-9 glass showed a more brittle behavior at 750 °C and 800 °C in comparison with the non-aged one because there was a less amount of viscous residual glass to release stresses. All of the non-aged, 100 h-aged, and 1000 h-aged GC-9 glass crystallized and became glass ceramic after the given sintering process and heat treatment. It is obvious that the crystalline phases in the 100 h-aged and 1000 h-aged GC-9 glass strengthen the high-temperature mechanical properties in comparison with the non-aged one. However, the residual glass phase still played a certain role in relaxing stresses at high temperature for all of the given sintered GC-9 glass.

In mechanical failure of a brittle material, the Weibull modulus is related to the shape, size, and distribution of strength-controlling flaws. A higher value of m indicates a less scattering in strength data and a smaller range of distribution in flaw size and shape. As shown in Table 3, the Weibull moduli for the given three aged conditions are comparable at 650 °C-800 °C. At room temperature, the non-aged condition has a m value lower than those of the two aged conditions. Apparently, outlines of the surface defects in the given three aged conditions at high temperatures are modified to a more consistent form due to the aforementioned crack healing effect.

3.1.4 Effect of environmental temperature on Young's modulus

The calculated Young's modulus (average value and standard deviation) based on Eq. (6) and the measured force-displacement relations for the given three aged conditions at various temperatures are shown in Table 4. The Young's modulus of the non-aged GC-9 glass barely changed when the temperature was increased from room temperature to 650 °C, but it was significantly reduced at 700 °C and above. It is obvious that the non-aged GC-9 glass lost its stiffness at 700 °C and above since some residual glass was present in the material. Note that the T_g of the aged bulk GC-9 glass is 650 °C [16]. Therefore, the stiffness of such a glass was reduced at 650 °C and above due to a significant change of viscosity. On the other hand, the 100 h-aged and 1000 h-aged GC-9 glass exhibited an increase of Young's modulus with temperature from room temperature to 700 °C. Above 700 °C, the Young's modulus of the 100 h-aged and 1000 h-aged GC-9 glass was decreased with increasing temperature and a sudden drop took place at 750 °C which is higher than that of 700 °C in the non-aged one. For a given temperature, the Young's modulus of the 100 h-aged GC-9 glass was slightly larger than that of the 1000 h-aged one. This might be due to that the microvoids in the 1000 h-aged GC-9 glass were more than those in the 100 h-aged one. Also note that for a given temperature, specimens of the two aged conditions always had a greater Young's modulus than the non-aged one due to a greater extent of crystallization.

3.1.5 Failure analysis

Typical fracture and cracking patterns in the ring-on-ring specimens of the 1000 h-aged, sintered GC-9 glass are shown in Figs. 15 and 16. Specimens of the 1000 h-aged GC-9 glass tested at 25 °C, 650 °C, and 700 °C were commonly broken into two pieces, while some specimens at 700 °C were broken into three pieces. Fracture of the specimen broken into two or three pieces is a type of low-energy failure according to ASTM C1499 (Fig. 17) [30]. The specimen broken into more pieces has a greater fracture strength. Such failure patterns of the 1000 h-aged GC-9 glass are similar to those of the non-aged and 100 h-aged ones [16] at temperature of 700 °C and below. From the fracture and cracking patterns, most of the 1000 h-aged GC-9 glass specimens exhibited low-energy failure patterns (Fig. 15), and only a few showed a medium-energy failure pattern at 750 °C, which was broken into four pieces (Fig. 16).

When the testing temperature was increased to 800 °C, surface cracks were generated and grew on the tensile surfaces of the unbroken 1000 h-aged GC-9 glass specimens, as shown in Fig. 18. Note that a large flexural deflection was also observed for this case. The 1000 h-aged GC-9 glass exhibited line surface cracks at 800 °C, similar to that in the 100 h-aged one [16]. Note that the surface cracks on the unbroken, non-aged specimens at 750 °C and 800 °C have a ring shape instead of line shape [16]. The difference in the failure pattern between the non-aged and aged (100 h- and 1000 h-aged) GC-9 glass at 750 °C and 800 °C was due to different extents of crystallization. The aged GC-9 glass showed a less ductility at 750 °C and 800 °C because of existence of more crystalline phases.

Figures 19-21 show the typical fracture origins of low- and medium-energy failure for the 1000 h-aged, sintered GC-9 glass. There were many pores with different sizes in the 1000 h-aged GC-9 glass. Strength of the 1000 h-aged GC-9 glass was sensitive to these inherent defects on the tensile surface. These defects on the tensile surface are stress concentrating sites which are potential fracture origin. The shape of these defects is irregular and their size is varied with specimen. In the medium-energy failure (Fig. 21), a crack was generated on the primary crack plane, and then other branching cracks were developed from this primary crack plane. This type of crack branching need more energy. There was no difference in the fracture origin morphology between the low- or medium-energy failure patterns of the 1000 h-aged GC-9 glass specimens and all fracture originated from the inherent pores on the tensile surface. Although the microstructure of the aged GC-9 glass was changed from the non-aged one by heat treatment at 750 °C for a longer aging time, such inherent pores were still the primary sites of fracture origin at all testing temperatures.

3.2 Joint of Glass-Ceramic Sealant and Metallic Interconnect

3.2.1 Effect of LSM coating on the joint strength

Figure 22 shows the shear and tensile strength at 800 °C for joint specimens with and without LSM coating. In Fig. 22, the height of a solid bar indicates the average strength and the ends of an error bar represent the maximum and minimum strength for each given condition. For HT900 specimens, the average shear and tensile strength was of 4.7 MPa and 12.7 MPa, respectively. On the other hand, the average shear and tensile strength was of 0.8 MPa and 1.0

MPa for the CHT900 specimens, respectively. Both shear and tensile strength of HT900 were greater than those of CHT900 at 800 °C. This result indicates that coating LSM on the Crofer 22 H interconnect would degrade the joint strength.

Figure 23 shows the failure patterns in the shear specimens of HT900 and CHT900 tested at 800 °C. For the HT900 specimens (Fig. 23(a)) [34], in addition to delamination at the interface between the glass ceramic and chromate (BaCrO_4), fracture also took place in the glass-ceramic substrate. On the other hand, fracture of the CHT900 specimens took place at the interface between the glass-ceramic substrate and BaCrO_4 layer (Fig. 23(b)). Optical and SEM micrographs of an outlined region of fracture surface without adhered glass ceramic in Fig. 23(b) are shown in Fig. 24. There are three distinct zones in the outlined region, as shown in Fig. 24(a). In Fig. 24(b), the three zones from top to bottom are the Crofer 22 H coated with LSM film, GC-9 glass ceramic, and chromate (BaCrO_4) layer, respectively. By means of EDS analysis, element distributions in these three zones are confirmed and shown in Fig. 25. A high intensity of Si was found in the region of glass ceramic, as shown in Fig. 25(f). The distributions of Cr, La, and Mn shown in Figs. 25(b), (c), and (d), respectively, agree with the corresponding layers. As shown in Fig. 25(e), a high intensity of Ba agrees with the corresponding BaCrO_4 layer. These results indicate that the fracture mode indeed involves delamination of the interface between the glass-ceramic substrate and BaCrO_4 chromate.

As shown in Fig. 26, fracture of the tensile HT900 specimen took place within the GC-9 glass ceramic layer (Fig. 26(a)), while it took place at the interface between the glass-ceramic substrate and BaCrO_4 layer for the tensile CHT900 specimen (Fig. 26(b)). This result indicates that joint strength accompanied with delamination at the interface between the glass-ceramic substrate and BaCrO_4 layer was weaker than that involving fracture within the glass ceramic substrate. Figure 27(a) [34] shows the SEM micrograph of a cross-sectional view of the interface between the GC-9 and Crofer 22 H in an HT900 joint specimen without LSM coating. Two distinct zones can be observed in Fig. 27(a). The upper zone is the glass-ceramic sealant, while the lower region is the Crofer 22 H. A good adhesion between the glass-ceramic sealant and Crofer 22 H is observed. A continuous and crack-free interface is present indicating a good physical compatibility between the two materials. SEM micrograph of a cross-section of the interface in CHT900 is shown in Fig. 27(b). For the CHT900 specimen, some microvoids were observed at the interface between GC-9 and LSM coating film. Before the joining treatment,

the LSM coating film on Crofer 22 H was amorphous and dense. During the joining treatment, the LSM coating film became a perovskite phase, which would cause a volume reduction. At the same time, BaCrO₄ chromate was gradually formed during joining treatment. When the LSM coating film and BaCrO₄ were joined together and their deformation were not compatible, microcracks started to form at the BaCrO₄ layer. Because of these microcracks, the tensile CHT900 specimens fractured at the interface between the glass-ceramic substrate and BaCrO₄ layer leading to a lower strength.

The distributions of elements in the interface between GC-9 and Crofer 22 H of CHT900 by EDS analysis are shown in Fig. 28. The scanned region is shown in Fig. 28(a). The distribution of Cr (Fig. 28(b)) is mainly located at the Crofer 22 H substrate, and diffusion of some Cr into the glass-ceramic layer is also observed. This is because there are microcracks in the LSM coating film and Cr can diffuse through these microcracks easily. At the regions supposed to be the LSM coating layer, the intensities of La and O (Figs. 28(c) and (d)) are relatively greater than that of Ba (Fig. 28(e)), as expected. In this regard, the LSM coating layer was confirmed. In Fig. 28(f), Si is present in both the glass ceramic and Crofer 22 H and has a high intensity of content at the glass-ceramic side, as expected.

3.2.2 Creep rupture behavior

Creep rupture characteristics of the HT900 joint specimens subjected to constant shear and tensile loads at 800 °C are shown in Fig. 29 by plotting the applied stress versus creep rupture time. For shear creep joint specimens (Fig. 29(a)), four constant loads (280 N, 200 N, 190 N, and 180 N) were applied. For tensile creep joint specimens (Fig. 29(b)), the applied constant loads included 100 N, 80 N, 70 N, and 60 N. As shown in Fig. 29, variation of the creep rupture time with applied stress for each loading mode was well correlated by a simple power law. The fitted equations and correlation coefficients for each loading mode in Fig. 29 are given as follows:

$$\text{shear loading: } \tau t_r^{0.081} = 1.74, \quad r^2 = 0.94 \quad (9)$$

$$\text{tensile loading: } \sigma t_r^{0.082} = 1.91, \quad r^2 = 0.98 \quad (10)$$

where τ and σ are the applied shear and tensile stresses in unit of MPa and t_r is time to rupture in unit of h. The high values of correlation coefficient indicate

that the creep rupture time for the joint specimen subjected to a constant shear or tensile load at 800 °C can be predicted through these power-law relations. As shown in Fig. 29(a), the creep rupture time increases with a decrease in applied stress for shear creep joint specimens. A similar phenomenon is observed for the tensile creep joint specimens (Fig. 29(b)). When the applied stress is about 1.6 MPa, the creep rupture time is smaller than 10 h for both loading modes. On the other hand, if the creep rupture time needs to be longer than 1000 h, the applied stress should be smaller than about 1 MPa for both loading modes. This applied shear stress level is about 21% of the average shear strength (4.7 MPa) [34]. In other words, the shear creep strength at 1000 h for the joint of GC-9 glass ceramic sealant and Crofer 22 H interconnect at 800 °C is about one fifth of the average shear strength. For tensile joint specimens, the tensile creep strength at 1000 h is only about 8% of the average tensile strength.

Figure 30 shows the failure patterns in the shear creep joint specimens tested at 800 °C. For the shear creep joint specimen with a shorter creep rupture time (< 100 h), creep fracture took place at the interface between the glass-ceramic substrate and BaCrO₄ layer (Fig. 30(a)). For a longer creep rupture time (> 500 h), fracture of the shear creep joint specimen took place both in the GC-9 glass ceramic sealant layer and at the interface between the glass ceramic and BaCrO₄ layers (Fig. 30(b)). It is thought that the crack initiated at one of the glass ceramic/chromate interfaces and propagated with partial delamination along this interface. Note that there are two layers of BaCrO₄ chromate formed on each side of the glass ceramic layer. At a certain stage of the creep testing, the crack went through the glass-ceramic layer. Once the crack reached the other glass ceramic/chromate interface, it propagated with partial delamination along this latter interface. The failure pattern of the shear creep joint specimens with a shorter creep rupture time (Fig. 30(a)) is similar to that of the shear joint strength test specimens. Shear fracture with cracking along the interface between the GC-9 glass ceramic and BaCrO₄ layers and through the glass ceramic layer apparently had a longer creep rupture time than did that only involving delamination at the glass ceramic/chromate interface. The failure patterns in the tensile creep joint specimens tested at 800 °C are shown in Fig. 31. Regardless of the applied stress level, fracture of all tensile creep joint specimens took place at the interface between the GC-9 glass ceramic substrate and BaCrO₄ layer. Note that the color of the GC-9 glass ceramic layer became darker when the creep rupture time was longer. Table 5 summarizes the fracture modes for various testing conditions given in the present study.

4. CONCLUSIONS

- (1) The extent of crystallization in the GC-9 glass ceramic sealant was increased with a longer aging time. In addition to the α -Ba($\text{Al}_2\text{Si}_2\text{O}_8$) phase, the dominant crystalline phases in the 1000 h-aged GC-9 glass include Ca($\text{Al}_2\text{Si}_2\text{O}_8$) and Al_2SiO_5 , as compared to the 100 h-aged and non-aged ones. A greater flexural strength and stiffness of the aged GC-9 glass over the non-aged one was observed at temperature higher than 700 °C due to a greater extent of crystallization.
- (2) T_g is an important factor for the variation of high-temperature mechanical properties in the 1000 h-aged, sintered GC-9 glass. There was a flexural strength improvement at high temperature below the inferred T_g (within 750 °C-800 °C), because of a crack healing effect from the residual glass in the material. Both flexural strength and Young's modulus were decreased at temperature above T_g .
- (3) According to the fractography analysis and flexural strength results, when a crack healing effect occurred, the GC-9 glass specimens needed more energy to fracture. When the testing temperature was around T_g and above, the residual glass had a lower viscosity and more energy was consumed in plastic deformation. Fracture of the sintered GC-9 glass specimens were initiated at inherent pores.
- (4) Coating of LSM on the Crofer 22 H interconnect resulted in a significant reduction of both tensile and shear joining strength of the glass ceramic/metallic interconnect joint specimens. It was attributed to formation of microvoids and microcracks in the BaCrO_4 chromate layer when the coated interconnect was joined with the glass ceramic sealant at high temperature.
- (5) For the joint specimens with LSM coating, fracture always took place at the interface between the GC-9 substrate and BaCrO_4 layer for both shear and tensile loading modes. For the shear joint specimens without LSM coating, fracture took place at the interface between the GC-9 substrate and BaCrO_4 layer and occasionally in the glass ceramic layer. Fracture always took place within the GC-9 layer for the tensile joint specimens without LSM coating.

- (6) For the joint specimens in creep test at 800 °C, the creep rupture time was shorter than 10 h when the applied stress was about 1.6 MPa in both shear and tensile loading modes. If the applied stress was smaller than 1 MPa, the creep rupture time was over than 1000 h for both shear and tensile joint specimens. The shear creep strength at 1000 h is about one fifth of the shear strength at 800 °C. The tensile creep strength at 1000 h is about eight percent of the tensile strength at 800 °C.
- (7) For the shear joint specimens with a longer creep rupture time, fracture took place at the glass ceramic/chromate interfaces accompanied with cracking through the glass ceramic layer. On the other hand, fracture took place at the interface between the glass-ceramic and BaCrO₄ layers in the shear joint specimens with a shorter creep rupture time. For the tensile joint specimens in creep test, fracture always took place at the interface between the glass-ceramic substrate and BaCrO₄ layer.

REFERENCES

1. W. Z. Zhu and S. C. Deevi, "A Review on the Status of Anode Materials for Solid Oxide Fuel Cells," *Materials Science and Engineering*, Vol. A362, pp. 228-239, 2003.
2. J. Malzbender, J. Mönch, R. W. Steinbrech, T. Koppitz, S. M. Gross, and J. Remmel, "Symmetric Shear Test of Glass-Ceramic Sealants at SOFC Operation Temperature," *Journal of Materials Science*, Vol. 42, pp. 6297-6301, 2007.
3. T. L. Wen, D. Wang, M. Chen, H. Tu, Z. Lu, Z. Zhang, H. Nie, and W. Huang, "Material Research for Planar SOFC Stack," *Solid State Ionics*, Vol. 148, pp. 513-519, 2002.
4. J. W. Fergus, "Sealants for Solid Oxide Fuel Cells," *Journal of Power Sources*, Vol. 147, pp. 46-57, 2005.
5. P. A. Lessing, "A Review of Sealing Technologies Applicable to Solid Oxide Electrolysis Cells," *Journal of Materials Science*, Vol. 42, pp. 3465-3476, 2007.
6. I. W. Donald, "Preparation, Properties and Chemistry of Glass- and Glass-Ceramic-to-Metal Seals and Coatings," *Journal of Materials Science*, Vol. 28, pp. 2841-2886, 1993.
7. V. A. Haanappel, V. Shemet, I. C. Vinke, and W. J. Quadackers, "A Novel Method to Evaluate the Suitability of Glass Sealant-Alloy Combinations under SOFC Stack Conditions," *Journal of Power Sources*, Vol. 141, pp. 102-107, 2005.
8. P. Batfalsky, V. A. C. Haanappel, J. Malzbender, N. H. Menzler, V. Shemet, I. C. Vinke, and R. W. Steinbrech, "Chemical Interaction Between Glass-Ceramic Sealants and Interconnect Steels in SOFC Stacks," *Journal of Power Sources*, Vol. 155, pp. 128-137, 2006.
9. S. Ghosh, A. D. Sharma, P. Kundu, and R. N. Basuz, "Glass-Ceramic Sealants for Planar IT-SOFC: A Bilayered Approach for Joining Electrolyte and Metallic Interconnect," *Journal of the Electrochemical Society*, Vol. 155, pp. 473-478, 2008.
10. K. S. Weil, J. E. Deibler, J. S. Hardy, D. S. Kim, G.-G. Xia, L. A. Chick, and C. A. Coyle, "Rupture Testing as a Tool for Developing Planar Solid

- Oxide Fuel Cell Seals,” *Journal of Materials Engineering and Performance*, Vol. 13, pp. 316-326, 2004.
11. S. R. Choi and N. P. Bansal, “Mechanical Properties of SOFC Seal Glass Composites,” *Ceramic Engineering and Science Proceedings*, Vol. 26, pp. 275-283, 2005.
 12. J. Milhans, M. Khaleel, X. Sun, M. Tehrani, M. Al-Haik, and H. Garmestani, “Creep Properties of Solid Oxide Fuel Cell Glass-Ceramic Seal G18,” *Journal of Power Sources*, Vol. 195, pp. 3631-3635, 2010.
 13. W. Liu, X. Sun, and M. A. Khaleel, “Predicting Young’s Modulus of Glass/Ceramic Sealant for Solid Oxide Fuel Cell Considering the Combined Effects of Aging, Micro-Voids and Self-Healing,” *Journal of Power Sources*, Vol. 185, pp. 1193-1200, 2008.
 14. Y.-S. Chou, J. W. Stevenson, and P. Singh, “Effect of Pre-Oxidation and Environmental Aging on the Seal Strength of a Novel High-Temperature Solid Oxide Fuel Cell (SOFC) Sealing Glass with Metallic Interconnect,” *Journal of Power Sources*, Vol. 184, pp. 238-244, 2008.
 15. E. V. Stephens, J. S. Vetrano, B. J. Koepfel, Y. Chou, X. Sun, and M. A. Khaleel, “Experimental Characterization of Glass-Ceramic Seal Properties and Their Constitutive Implementation in Solid Oxide Fuel Cell Stack Models,” *Journal of Power Sources*, Vol. 193, pp. 625-631, 2009.
 16. H.-T. Chang, “High-Temperature Mechanical Properties of a Glass Sealant for Solid Oxide Fuel Cell,” Ph.D. Thesis, National Central University, 2010.
 17. C.-K. Lin, T.-T. Chen, Y.-P. Chyou, and L.-K. Chiang, “Thermal Stress Analysis of a Planar SOFC Stack,” *Journal of Power Sources*, Vol. 164, pp. 238-251, 2007.
 18. A.-S. Chen, “Thermal Stress Analysis of a Planar SOFC Stack with Mica Sealants,” M.S. Thesis, National Central University, 2007.
 19. C.-K. Lin, L.-H. Huang, L.-K. Chiang, and Y.-P. Chyou, “Thermal Stress Analysis of a Planar Solid Oxide Fuel Cell Stacks: Effects of Sealing Design,” *Journal of Power Sources*, Vol. 192, pp. 515-524, 2009.
 20. F. Smeacetto, M. Salvo, M. Ferraris, V. Casalegno, P. Asinari, and A. Chrysanthou, “Characterization and Performance of Glass-Ceramic Sealant to Join Metallic Interconnects to YSZ and Anode-Supported-Electrolyte in

- Planar SOFCs,” *Journal of the European Ceramic Society*, Vol. 28, pp. 2521-2527, 2008.
21. Y.-S. Chou, J. W. Stevenson, and P. Singh, “Effect of Aluminizing of Cr-Containing Ferritic Alloys on the Seal Strength of a Novel High-Temperature Solid Oxide Fuel Cell Sealing Glass,” *Journal of Power Sources*, Vol. 185, pp. 1001-1008, 2008.
 22. F. Smeacetto, M. Salvo, M. Ferraris, J. Cho, and A.R. Boccaccini, “Glass-Ceramic Seal to Join Crofer 22 APU Alloy to YSZ Ceramic in Planar SOFCs,” *Journal of the European Ceramic Society*, Vol. 28, pp. 61-68, 2008.
 23. M. Stanislowski, J. Froitzheim, L. Niewolak, W.J. Quadackers, K. Hilpert, T. Markus, and L. Singheiser, “Reduction of Chromium Vaporization from SOFC Interconnectors by Highly Effective Coatings,” *Journal of Power Sources*, Vol. 164, pp. 578-589, 2007.
 24. S. Geng, J. Zhua, M. P. Brady, H. U. Anderson, X.-D. Zhou, and Z. Yang, “A Low-Cr Metallic Interconnect for Intermediate-Temperature Solid Oxide Fuel Cells,” *Journal of Power Sources*, Vol. 172, pp. 775-781, 2007.
 25. E. Konyshева, J. Laatsch, E. Wessel, F. Tietz, N. Christiansen, L. Singheiser, and K. Hilpert, “Influence of Different Perovskite Interlayers on the Electrical Conductivity Between $\text{La}_{0.65}\text{Sr}_{0.3}\text{MnO}_3$ and Fe/Cr-Based Steels,” *Solid State Ionics*, Vol. 177, pp. 923-930, 2006.
 26. D.-J. Jan, C.-T. Lin, and C.-F. Ai, “Structural Characterization of $\text{La}_{0.67}\text{Sr}_{0.33}\text{MnO}_3$ Protective Coatings for Solid Oxide Fuel Cell Interconnect Deposited by Pulsed Magnetron Sputtering” *Thin Solid Film*, Vol. 516, pp. 6300-6304, 2008.
 27. C.-K. Liu, T.-Y. Yung, and K.-F. Lin, “Effect of La Addition on the Thermal and Crystalline Properties of $\text{SiO}_2\text{-B}_2\text{O}_3\text{-Al}_2\text{O}_3\text{-BaO}$ Glasses,” *Proceedings of the Annual Conference of the Chinese Ceramic Society*, 2007 (CD-ROM). (in Chinese)
 28. C.-K. Liu, T.-Y. Yung, S.-H. Wu, and K.-F. Lin, “Study on a $\text{SiO}_2\text{-B}_2\text{O}_3\text{-Al}_2\text{O}_3\text{-BaO}$ Glass System for SOFC Applications,” *Proceedings of the MRS_Taiwan Annual Meeting*, 2007 (CD-ROM). (in Chinese)
 29. C.-K. Liu, T.-Y. Yung, and K.-F. Lin, “Isothermal Crystallization Properties of $\text{SiO}_2\text{-B}_2\text{O}_3\text{-Al}_2\text{O}_3\text{-BaO}$ Glass,” *Proceedings of the Annual*

- Conference of the Chinese Ceramic Society, 2008 (CD-ROM). (in Chinese)*
30. “Standard Test Method for Monotonic Equibiaxial Flexural Strength of Advanced Ceramics at Ambient Temperature,” *ASTM Standard C1499*, ASTM International, West Conshohocken, PA, USA, 2008.
 31. R. W. Schmitt, K. Blank, and G. Schönbrunn, “Experimentelle Spannungsanalyse zum Doppelringverfahren,” *Sprechsaal*, Vol. 116, pp. 397-409, 1983. (in German)
 32. D. W. Richerson, *Modern Ceramic Engineering*, 2nd ed., Marcel Dekker, Inc., New York, USA, 1992.
 33. Y.-T. Chiou, private communication, 2010.
 34. J.-Y. Chen, “Analysis of Mechanical Properties for the Joint of Metallic Interconnect and Glass Ceramic in Solid Oxide Fuel Cell,” M.S. Thesis, National Central University, 2010.
 35. B. N. Nguyen, B. J. Koeppel, S. Ahzi, M. A. Khaleel, and P. Singh, “Crack Growth in Solid Oxide Fuel Cell Materials: From Discrete to Continuum Damage Modeling,” *Journal of the American Ceramic Society*, Vol. 89, pp. 1358-1368, 2006.

Table 1 Chemical composition of Crofer 22 H alloy (in wt.%)

Fe	C	Cr	Mn	Si	Ti	Nb
Bal.	0.007	22.93	0.43	0.21	0.07	0.51
Cu	S	P	Al	W	La	
0.02	<0.002	0.014	0.02	1.94	0.08	

Table 2 Mechanical property of Crofer 22 H alloy [33]

Temperature (°C)	Yield Strength (MPa)	Ultimate Tensile Strength (MPa)	Young's Modulus (GPa)	Elongation (in 12 mm) (%)
25	406	567	205	27
600	286	359	181	29
650	241	295	161	30
700	204	219	142	39
750	140	147	88	54
800	120	123	86	55

Table 3 Weibull characteristic strength (σ_0) and Weibull modulus (m) for variously aged GC-9 glass at different temperatures

		Temperature				
Aged condition		25 °C	650 °C	700 °C	750 °C	800 °C
σ_0 (MPa)	Non-aged	42	54	51	36	19
	100 h-aged	41	53	63	59	34
	1000 h-aged	49	67	61	64	38
m	Non-aged	4	5.2	5	6	5.8
	100 h-aged	5.5	5	4.8	4.9	6
	1000 h-aged	6.5	4.8	4.2	5.4	5.3

(Note that data of the non-aged and 100 h-aged conditions are taken from Ref. [16].)

Table 4 Average flexural strength and Young's modulus for variously aged GC-9 glass at different temperatures

	Aged condition	Temperature				
		25 °C	650 °C	700 °C	750 °C	800 °C
Flexural strength (MPa)	Non-aged	38 (9.9)	50 (10.1)	47 (9.3)	33 (5.5)	18 (3.1)
	100 h-aged	38 (6.7)	49 (9.9)	53 (11.2)	54 (10.2)	32 (5.5)
	1000 h-aged	45 (6.8)	59 (11.8)	49 (15.6)	57 (14.6)	36 (6.7)
Young's modulus (GPa)	Non-aged	18 (5.8)	19 (3.3)	9.4 (2.2)	4.9 (1.9)	2.1 (0.7)
	100 h-aged	19 (4.2)	24 (4.0)	31 (4.2)	17 (2.4)	6.5 (1.1)
	1000 h-aged	16 (3.3)	21 (4.4)	22 (4.4)	15 (3.7)	6 (2.1)

Note: value in the parentheses is the standard deviation.

(Note that data of the non-aged and 100 h-aged conditions are taken from Ref. [16].)

Table 5 Fracture site of tested shear and tensile joint specimens

Specimen condition	Fracture site*
Shear joint specimen of HT900	A+B
Shear joint specimen of CHT900	B
Tensile joint specimen of HT900	A
Tensile joint specimen of CHT900	B
Shear creep joint specimen with shorter rupture time	B
Shear creep joint specimen with longer rupture time	A+B
Tensile creep joint specimen with shorter rupture time	B
Tensile creep joint specimen with longer rupture time	B

*A: in glass-ceramic sealant layer; B: at the interface between the glass-ceramic substrate and BaCrO₄ layer.

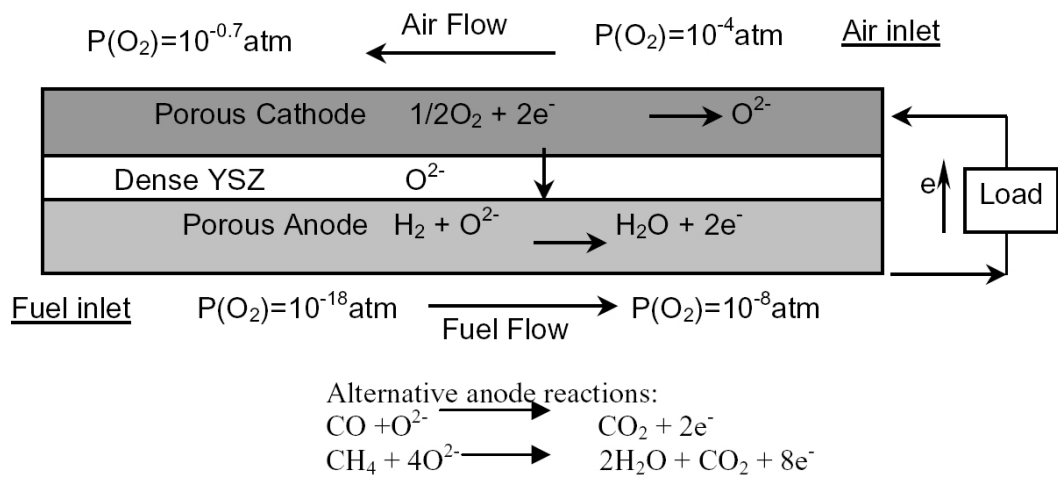


Fig. 1 Schematic of working principle for SOFC operating with hydrogen. [1]

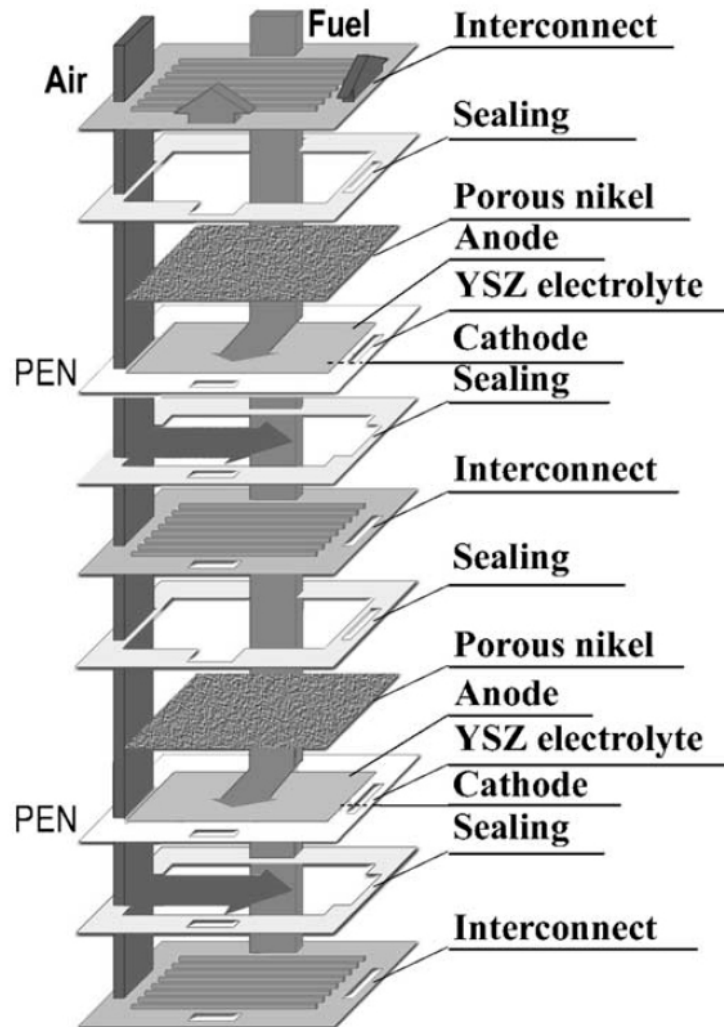


Fig. 2 Structural scheme of a planar SOFC stack. [3]

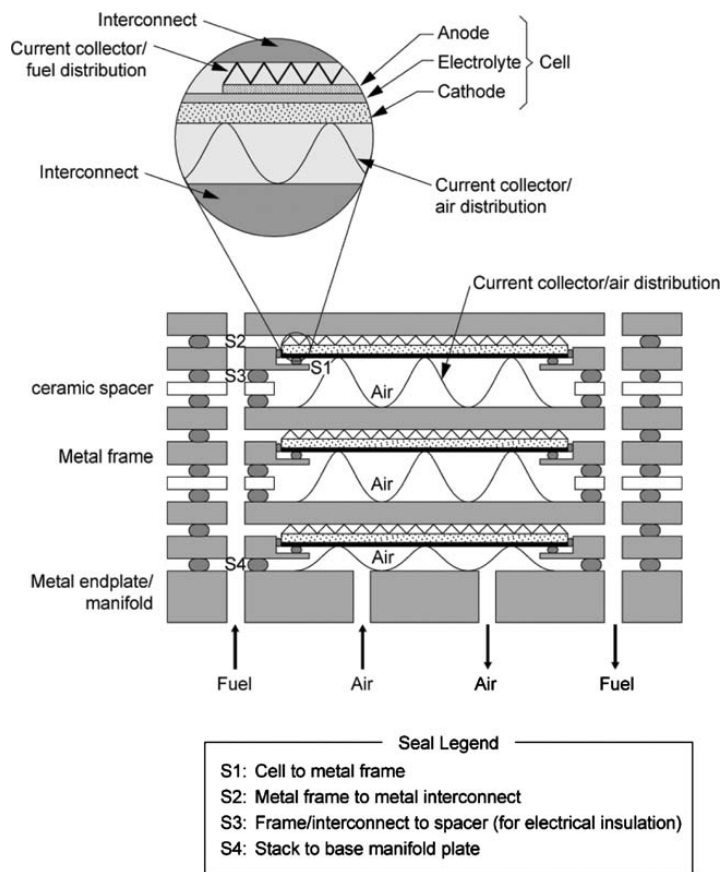


Fig. 3 Scheme of seals used in a planar SOFC stack with metallic interconnects and metallic internal gas manifold channels. [5]

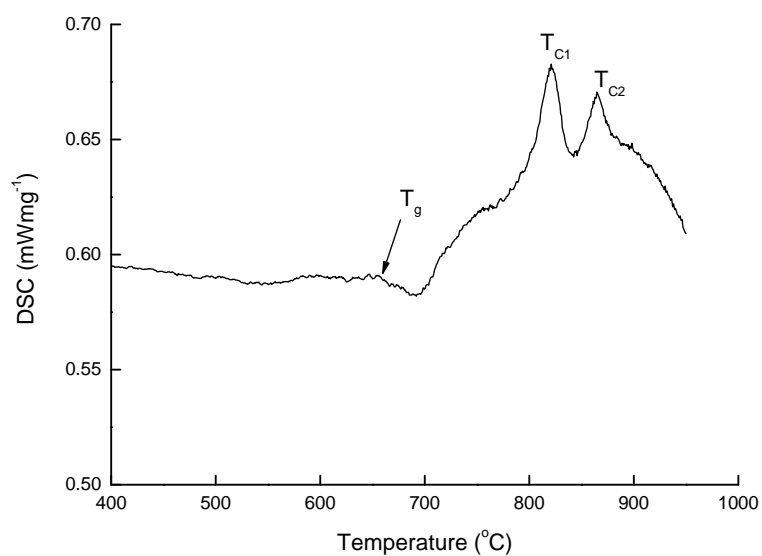


Fig. 4 DSC thermograph of non-aged bulk GC-9. [27]

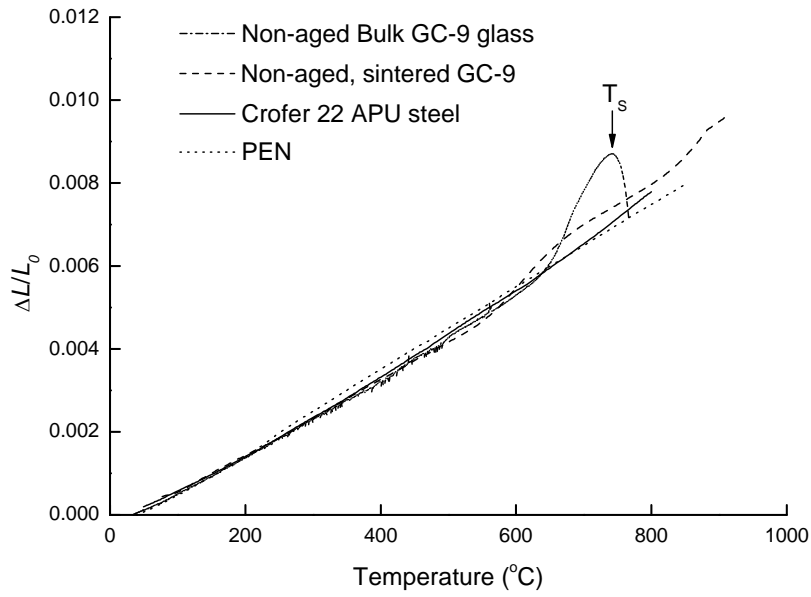


Fig. 5 Thermal expansion curves of non-aged bulk GC-9, non-aged, sintered GC-9, Crofer 22 APU, and PEN. [29]

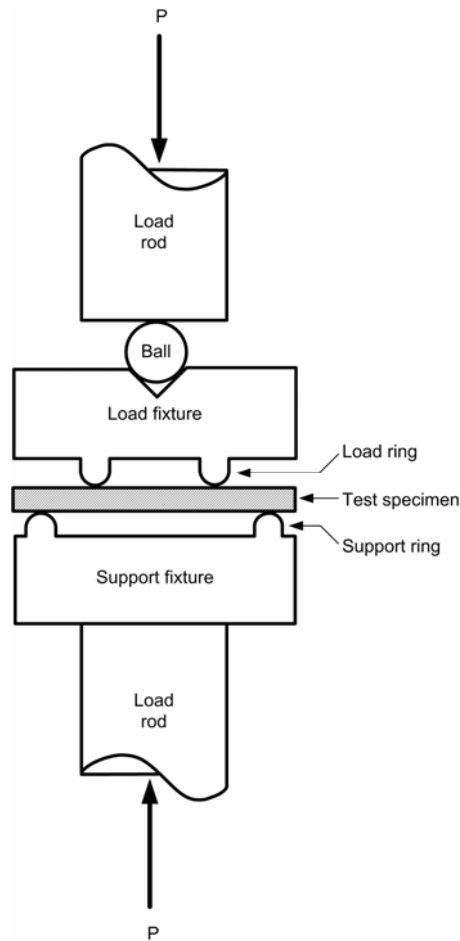


Fig. 6 Schematic of ring-on-ring test fixture.

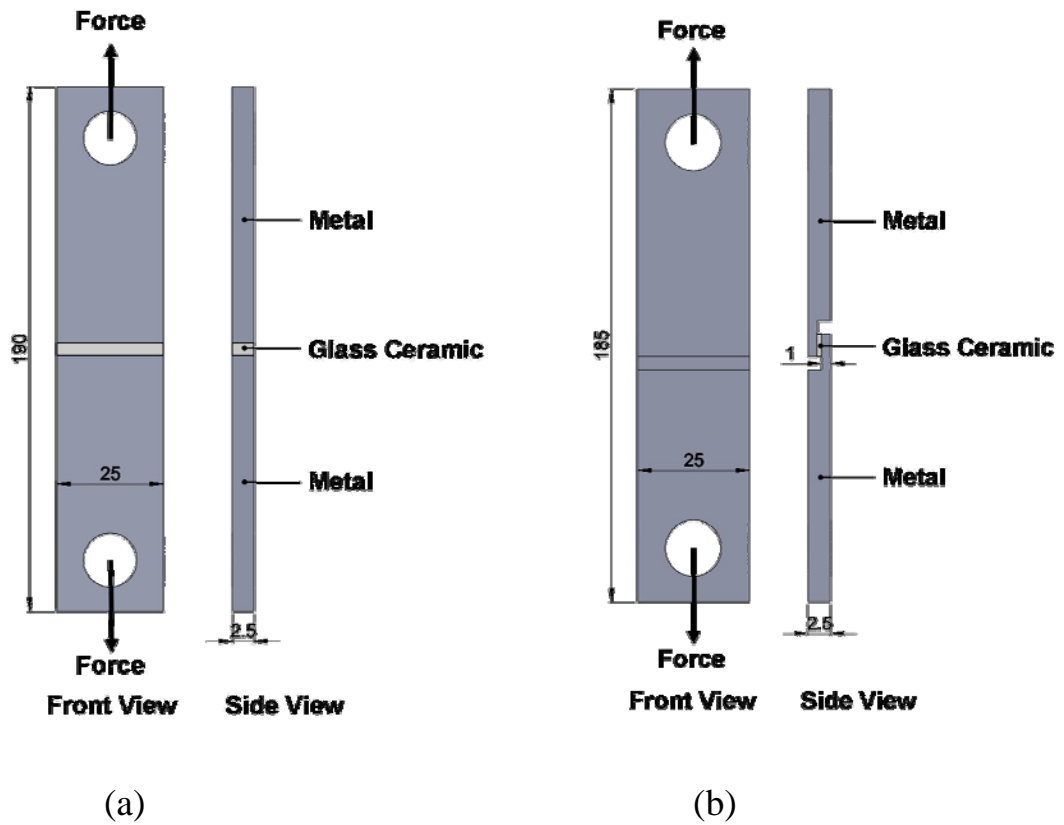


Fig. 7 Scheme of two types of joint specimens: (a) tensile specimen and (b) shear specimen. (Dimensions: mm)

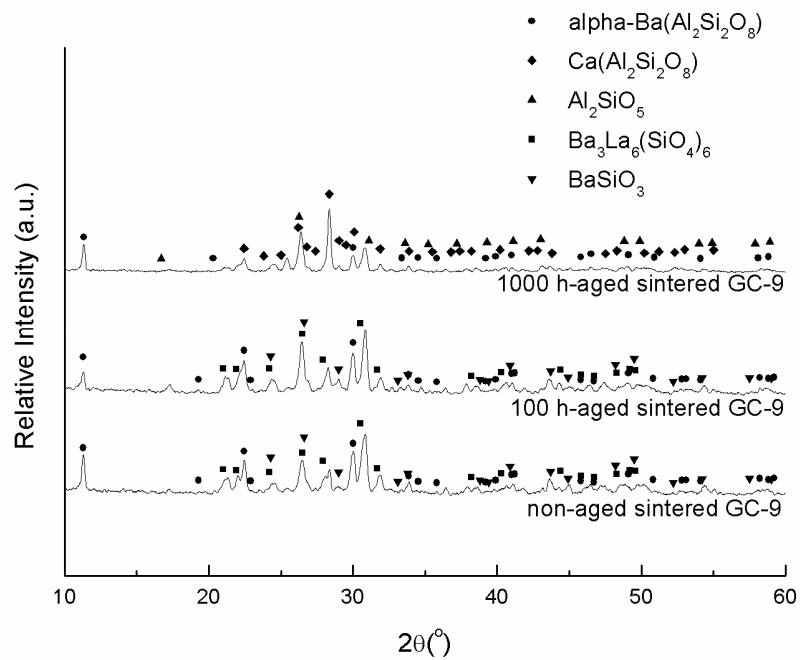
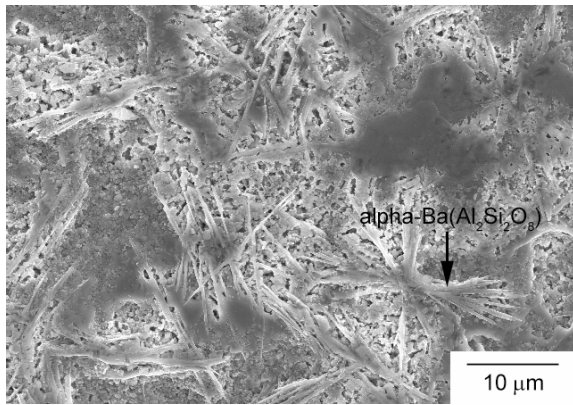
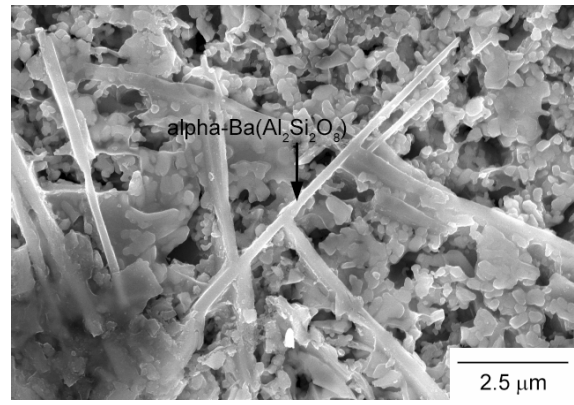


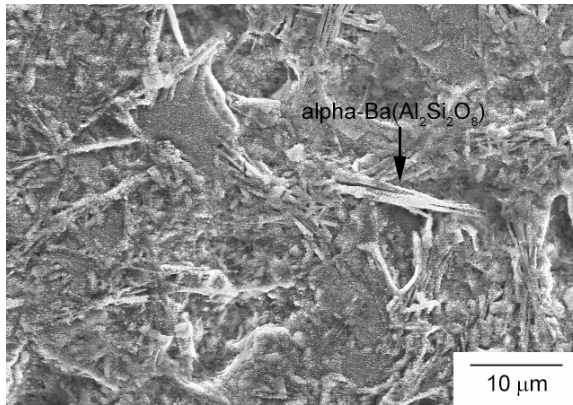
Fig. 8 XRD patterns of GC-9 glass in various conditions. (Note data of the non-aged and 100 h-aged conditions are taken from Ref. [16].)



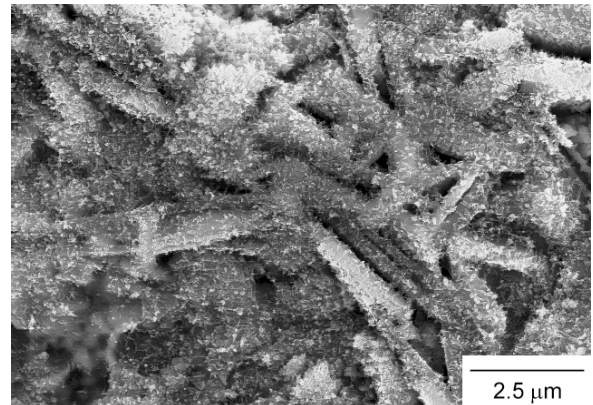
(a)



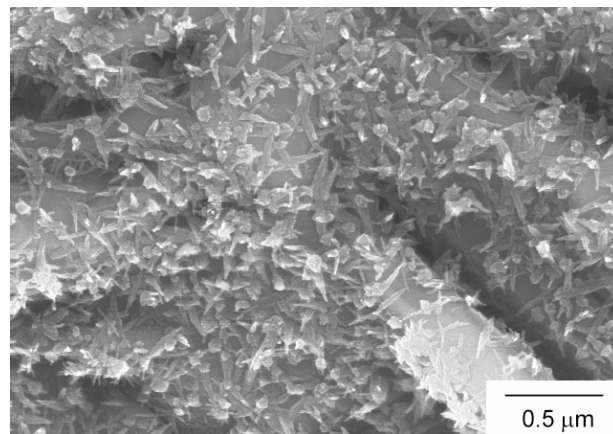
(b)



(c)

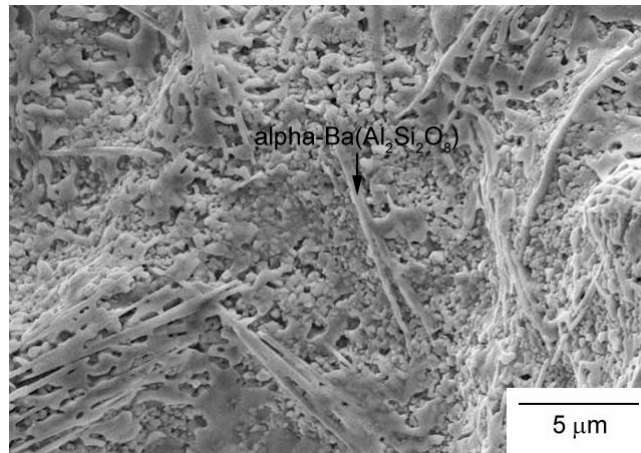


(d)

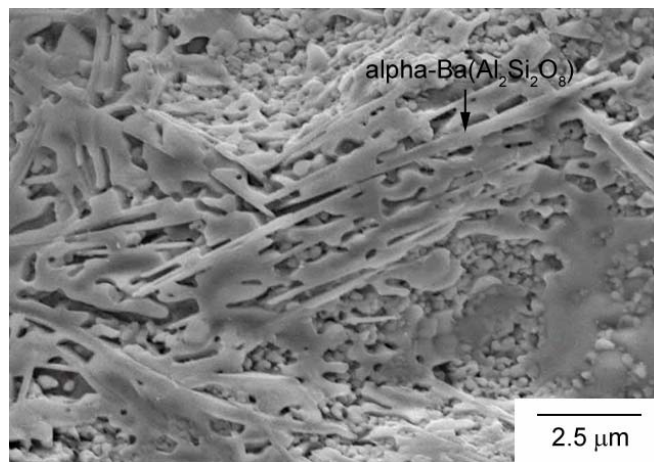


(e)

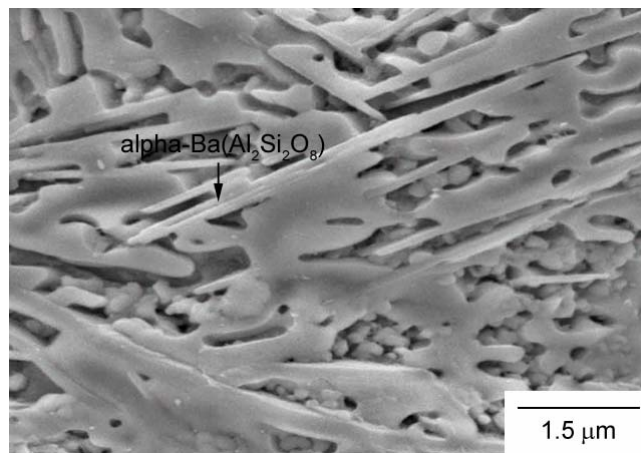
Fig. 9 Microstructure of sintered GC-9 glass: (a) non-aged; (b) non-aged in high magnification; (c) 100 h-aged; (d) 100 h-aged in high magnification; (e) 100 h-aged in higher magnification. [16]



(a)

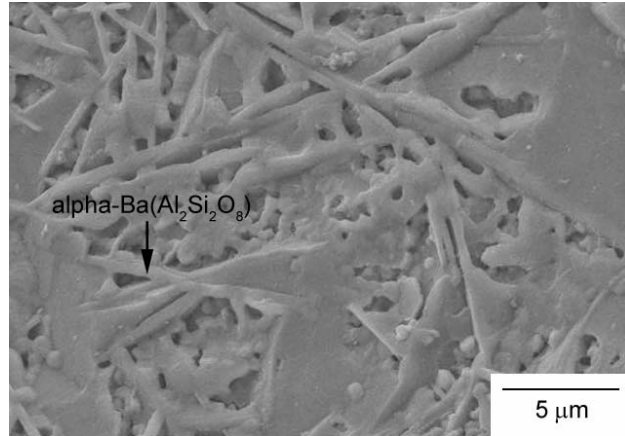


(b)

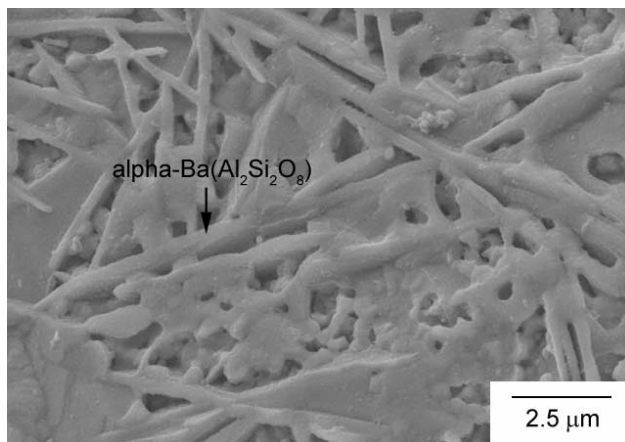


(c)

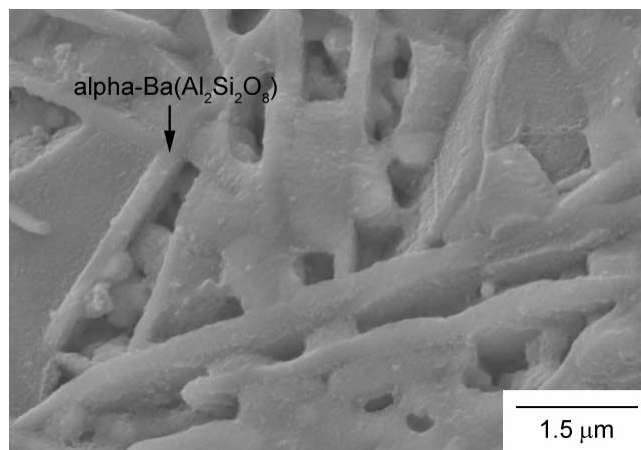
Fig. 10 Microstructure of 100 h-aged, sintered GC-9 glass: (a) low magnification; (b) high magnification; (c) higher magnification.



(a)

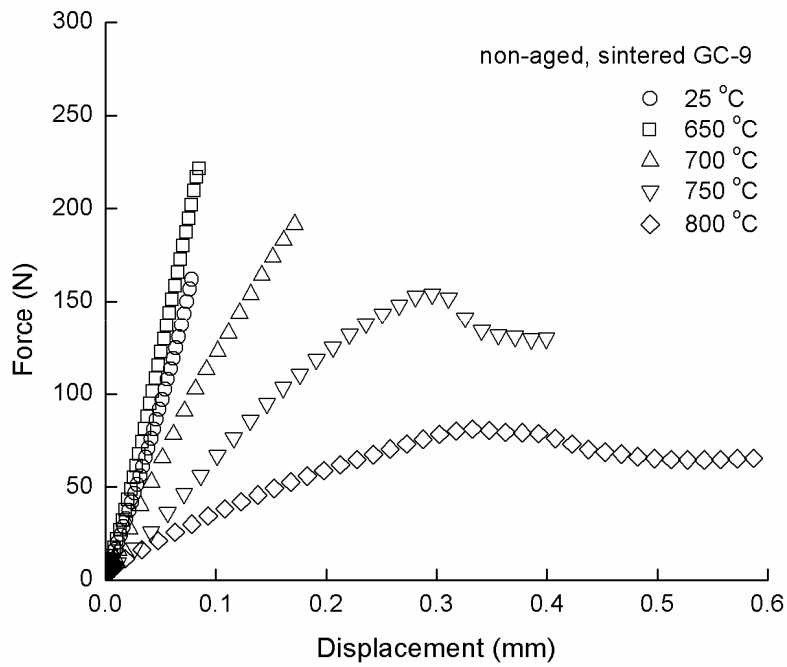


(b)

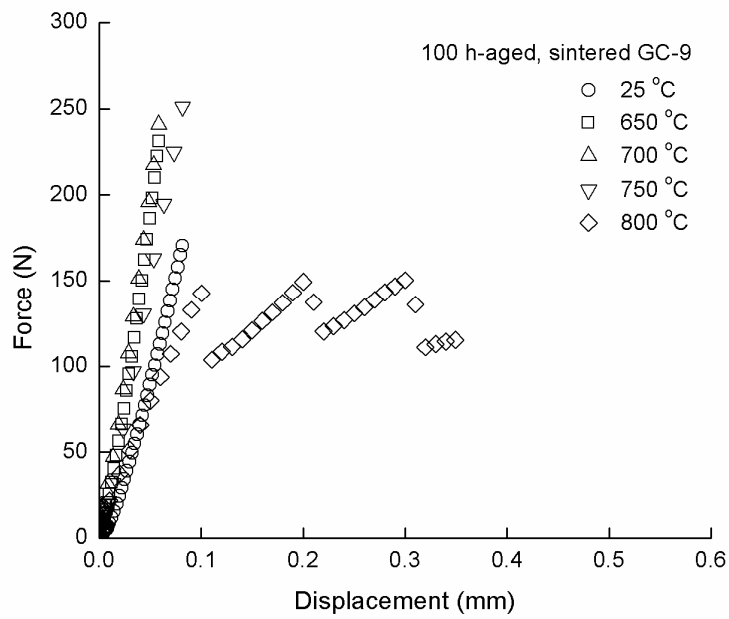


(c)

Fig. 11 Microstructure of 1000 h-aged, sintered GC-9 glass: (a) low magnification; (b) high magnification; (c) higher magnification.

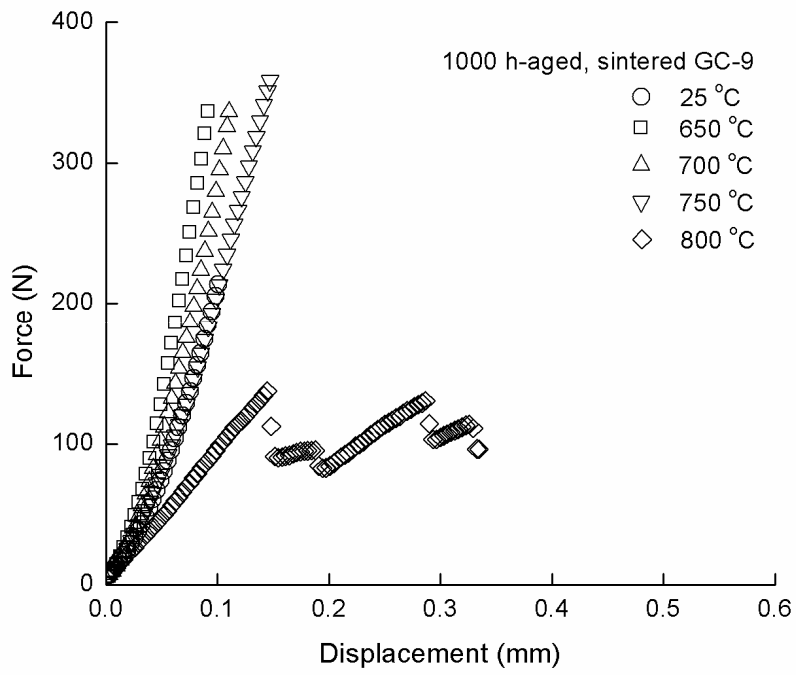


(a)



(b)

Fig. 12 Typical force-displacement relationships under a displacement rate of 0.0005 mms^{-1} at various temperatures for (a) non-aged [16], (b) 100 h-aged [16], and (c) 1000 h-aged, sintered GC-9 glass.



(c)

Fig. 12 (continued)

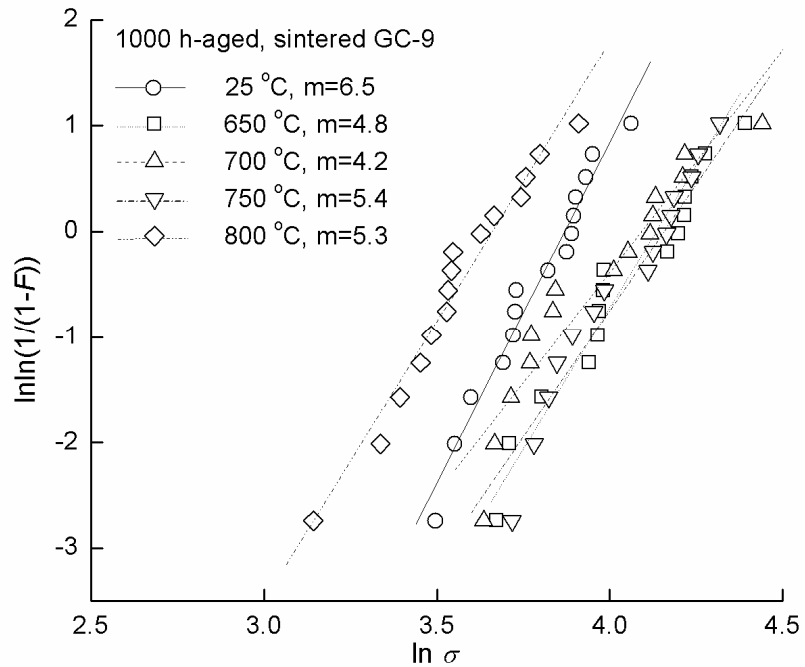


Fig. 13 Weibull distribution of flexural strength for 1000 h-aged, sintered GC-9. (The unit of σ is MPa)

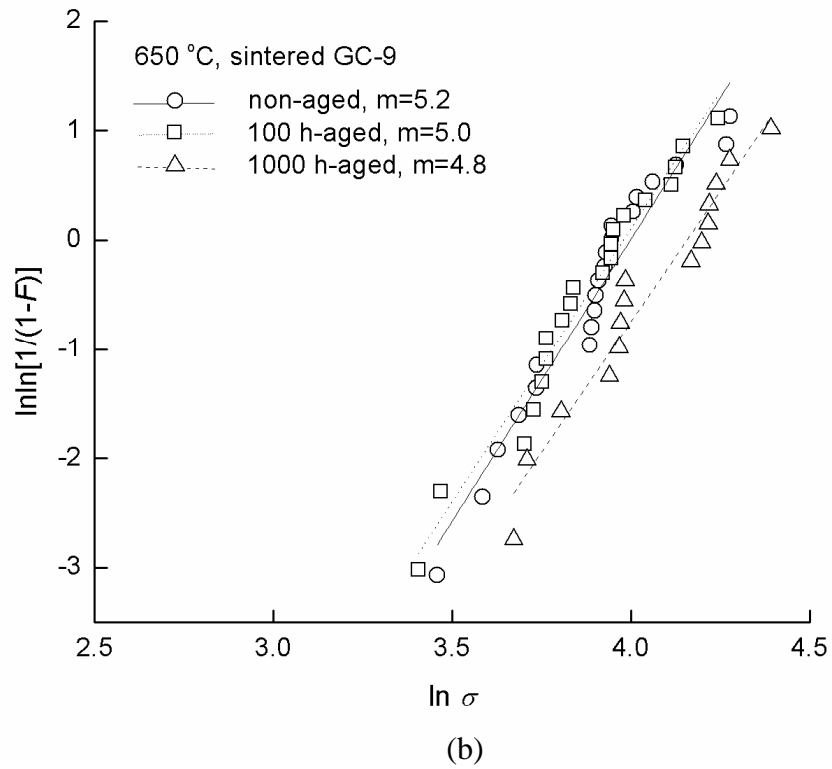
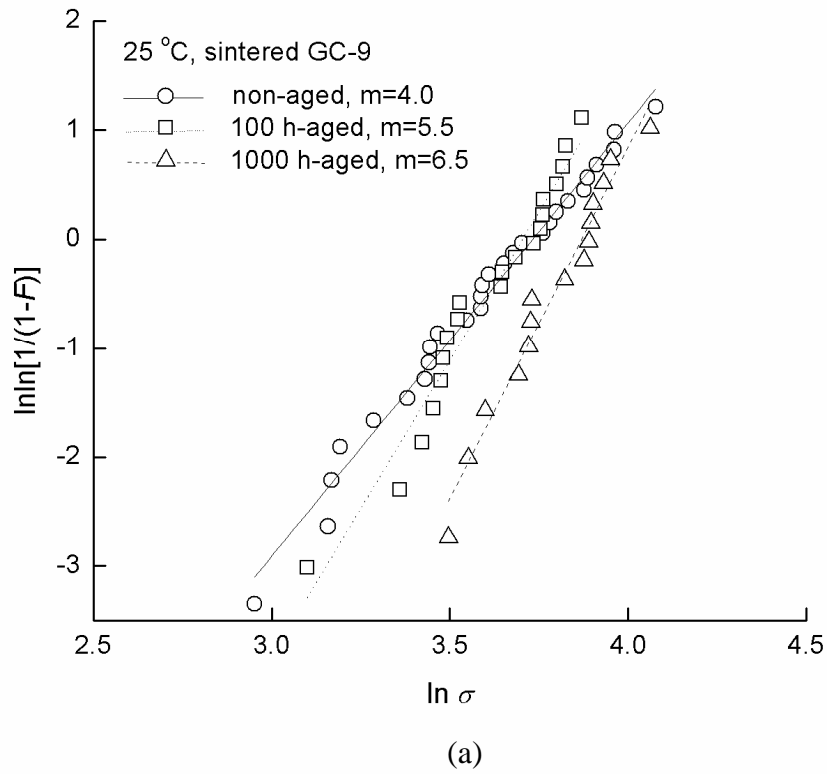
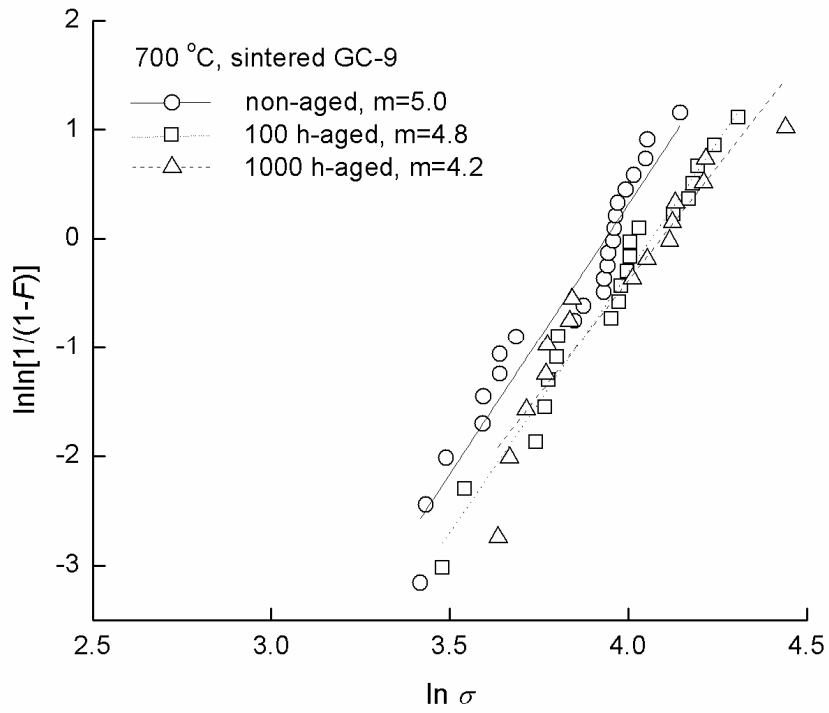
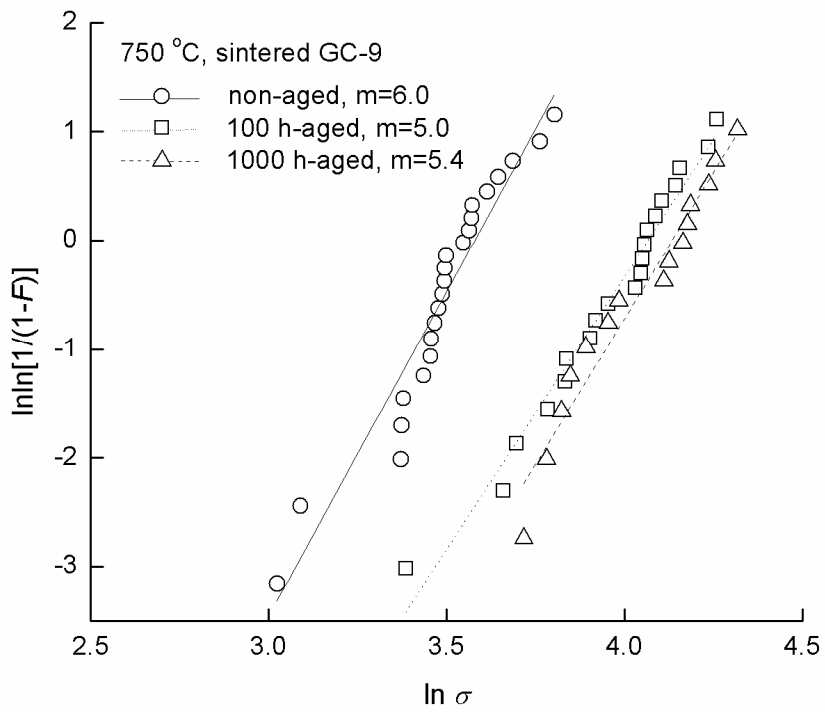


Fig. 14 Weibull distribution of flexural strength for non-aged, 100 h-aged, and 1000 h-aged, sintered GC-9 glass at various testing temperatures: (a) 25 °C, (b) 650 °C, (c) 700 °C, (d) 750 °C, and (e) 800 °C. (The unit of σ is MPa. Data of the non-aged and 100 h-aged conditions are taken from Ref. [16].)



(c)



(d)

Fig. 14 (continued)

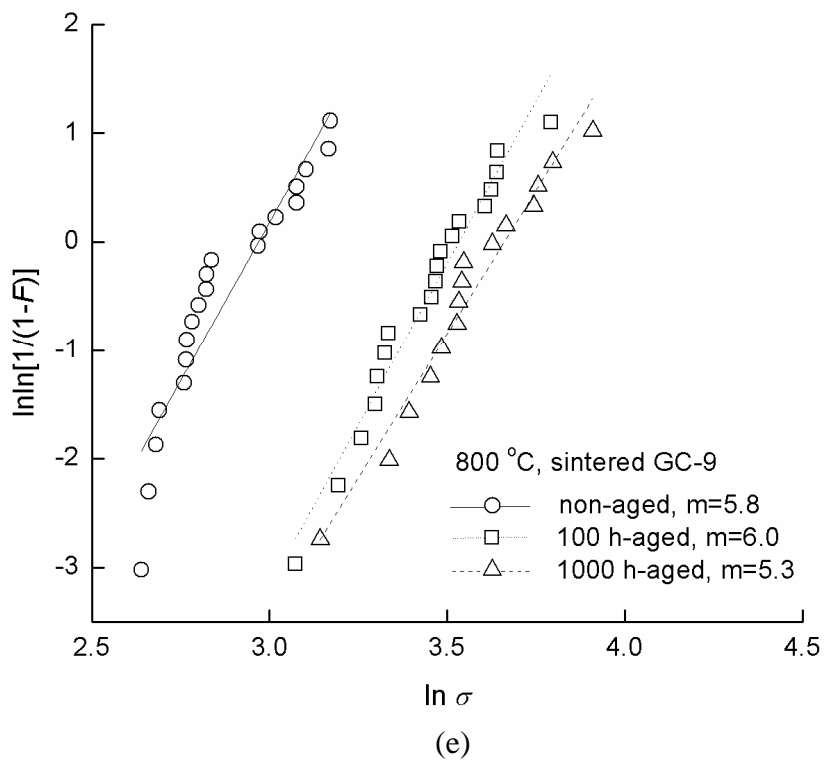


Fig. 14 (continued)

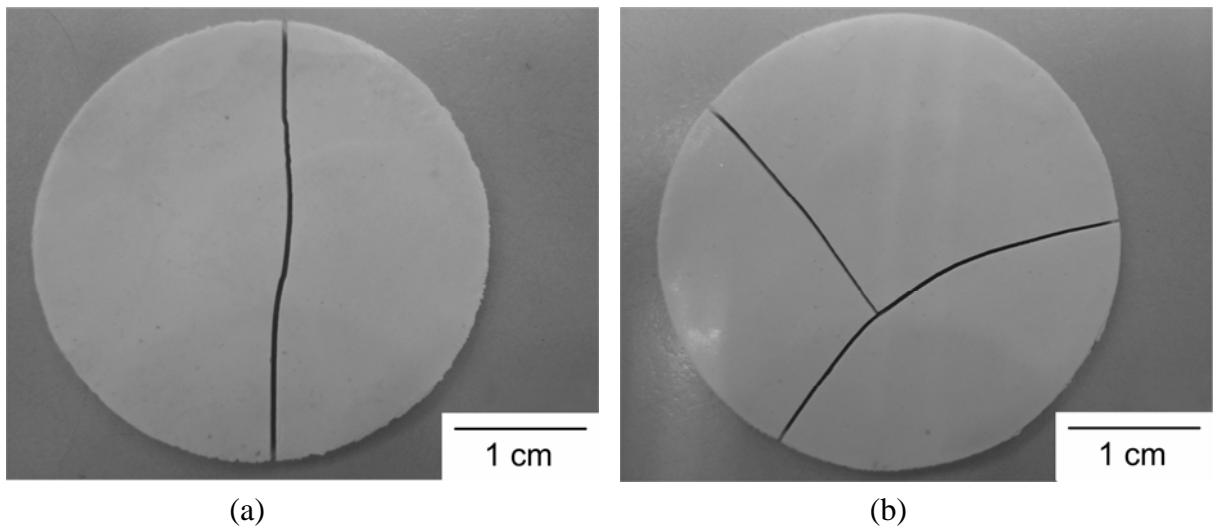


Fig. 15 Typical low-energy failure patterns in the ring-on-ring specimens of the 1000 h-aged GC-9 glass: (a) 2-piece fracture; (b) 3-piece fracture.

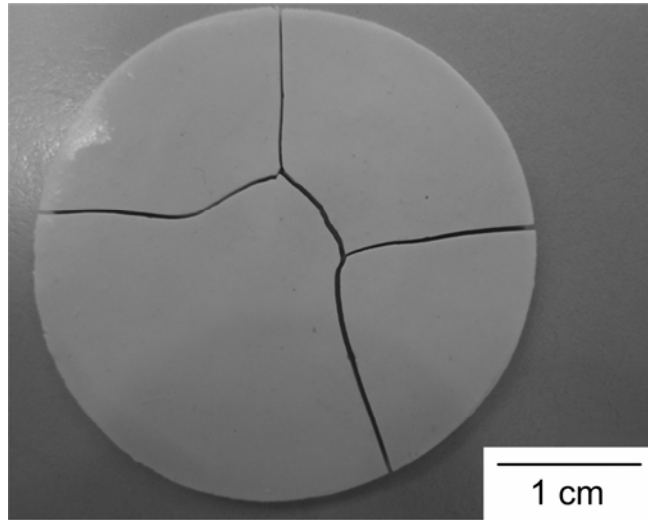


Fig. 16 Typical medium-energy failure pattern in the ring-on-ring specimens of the 1000 h-aged GC-9 glass.

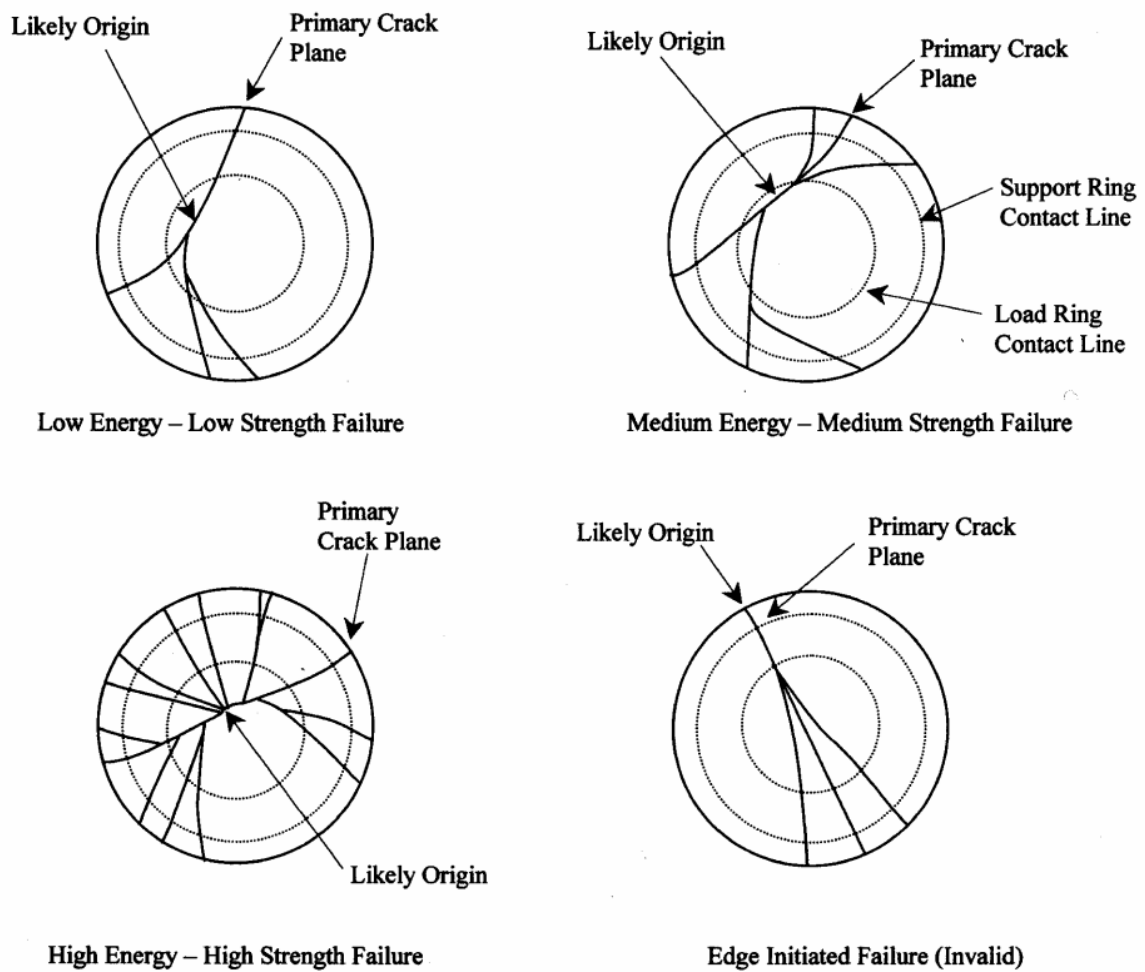


Fig. 17 Illustrations of failure patterns in concentric ring test specimens. [30]

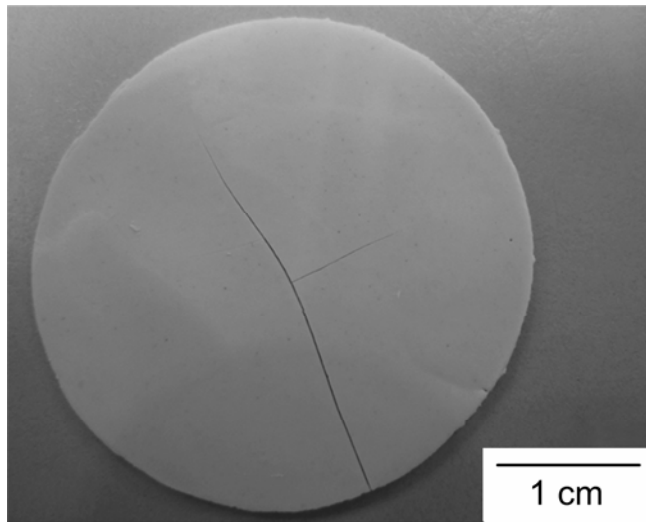
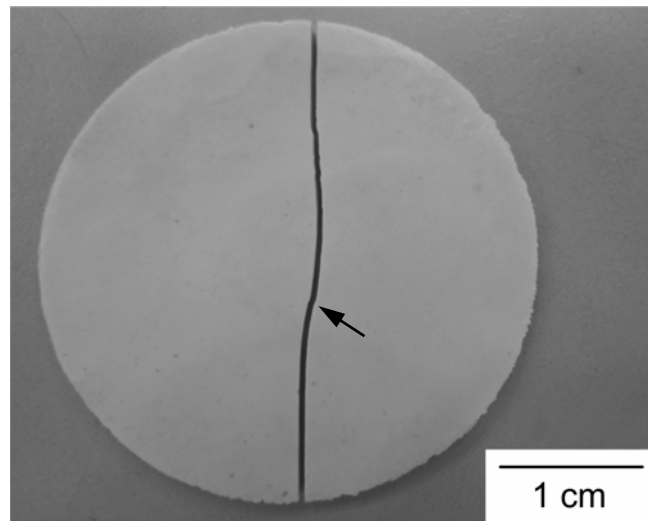
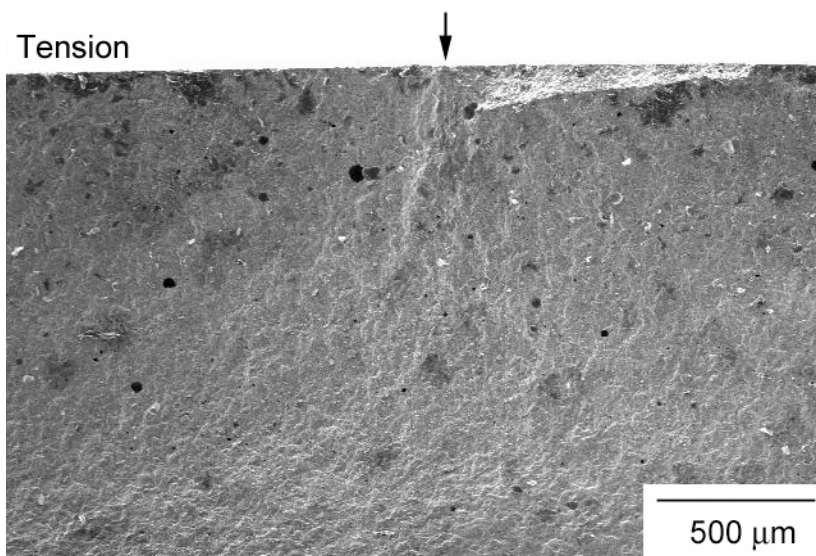


Fig. 18 Typical cracking patterns in the 1000 h-aged GC-9 glass specimens tested at 800 °C.

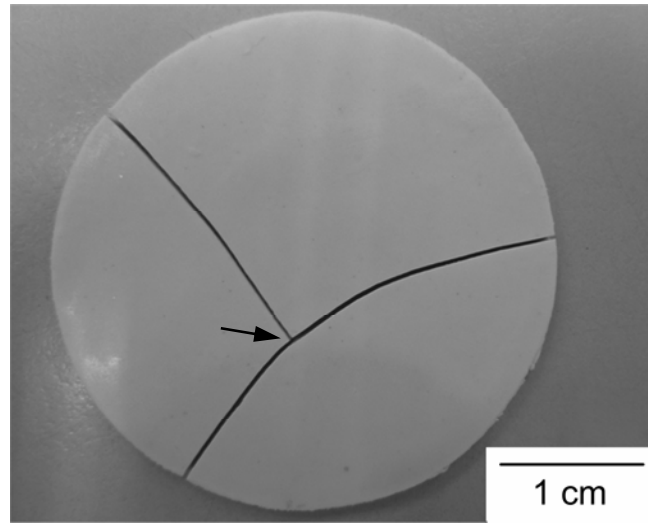


(a)

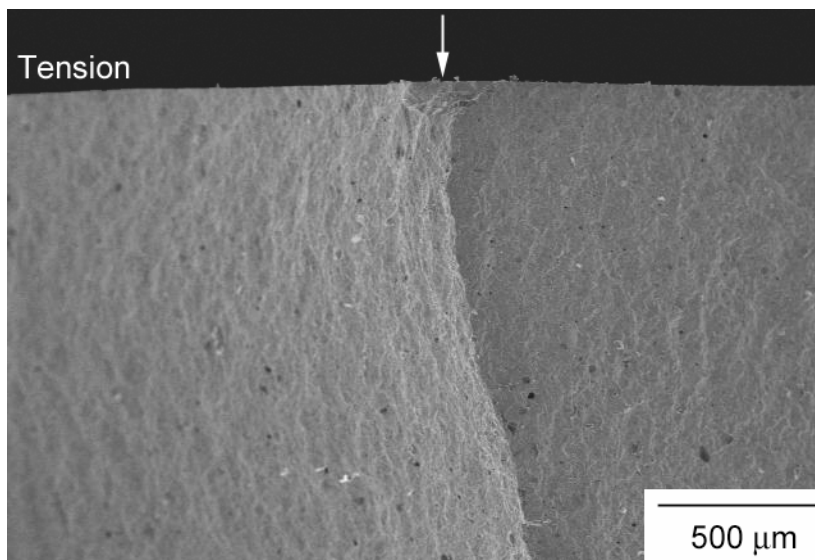


(b)

Fig. 19 Typical 2-piece low-energy fracture in the 1000 h-aged GC-9 glass: (a) fracture origin location on the tensile surface; (b) fracture origin on the fracture surface. (Arrows indicate the fracture origin.)

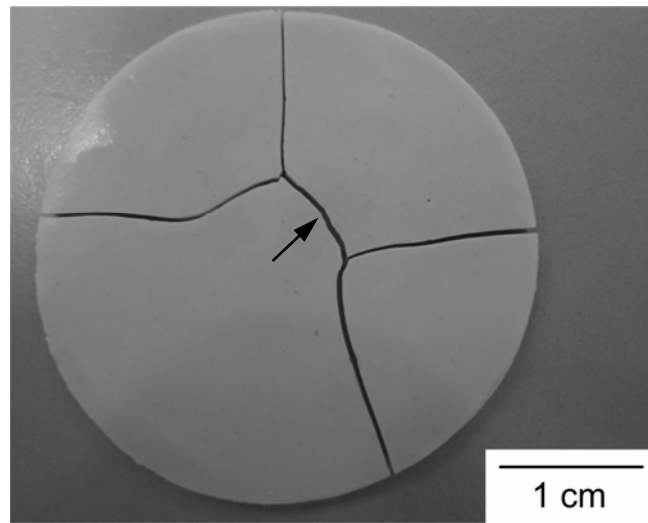


(a)

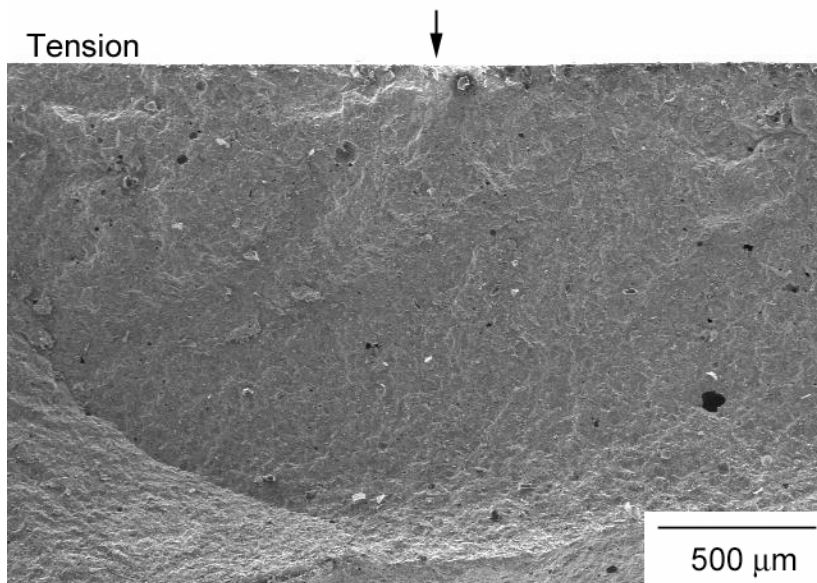


(b)

Fig. 20 Typical 3-piece low-energy fracture in the 1000 h-aged GC-9 glass: (a) fracture origin location on the tensile surface; (b) fracture origin on the fracture surface. (Arrows indicate the fracture origin.)

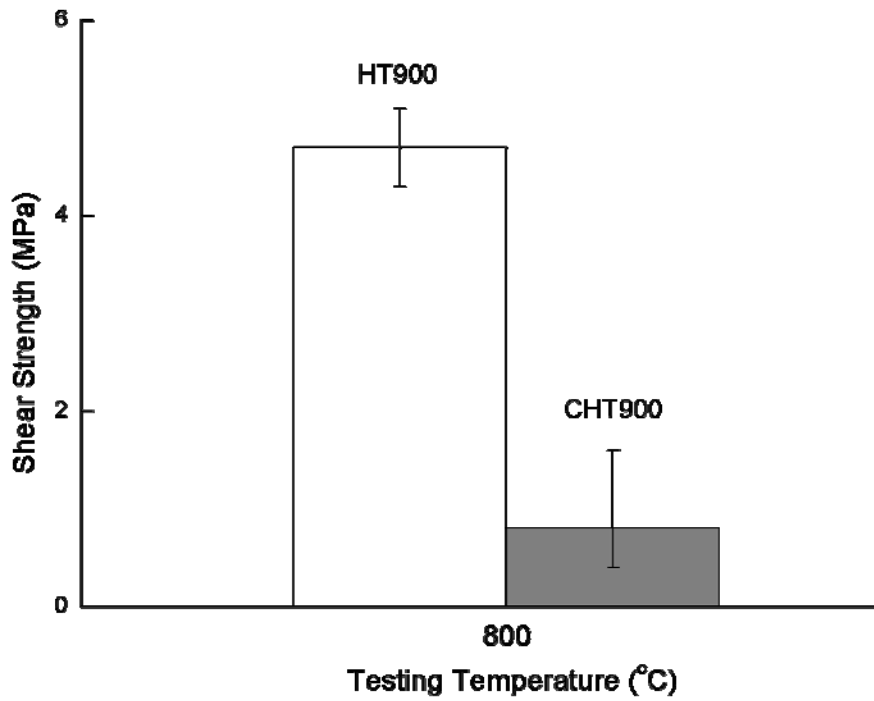


(a)

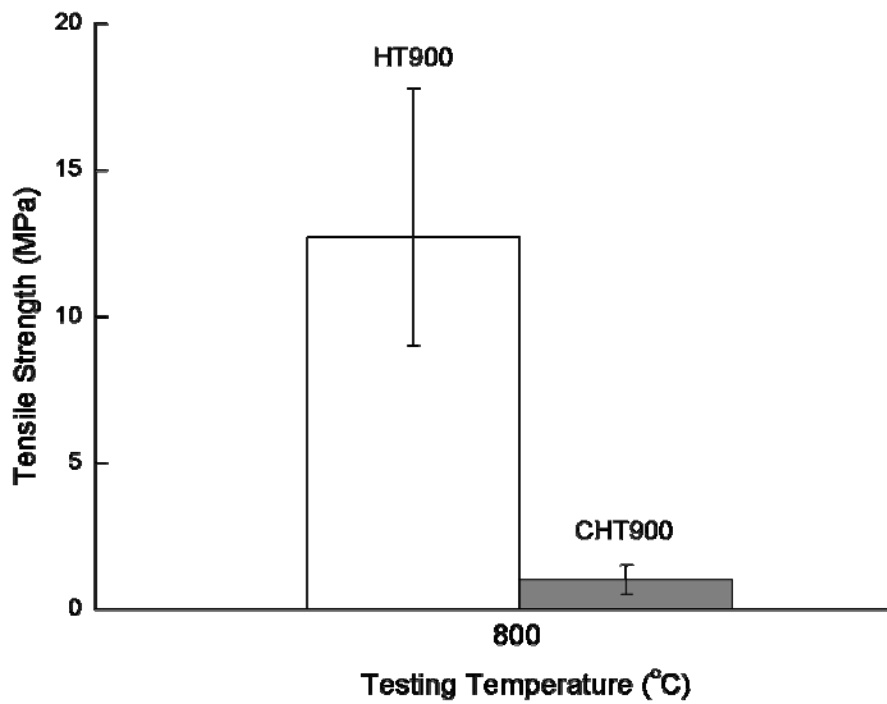


(b)

Fig. 21 Typical 4-piece medium-energy fracture in the 1000 h-aged GC-9 glass: (a) fracture origin location on the tensile surface; (b) fracture origin on the fracture surface. (Arrows indicate the fracture origin.)

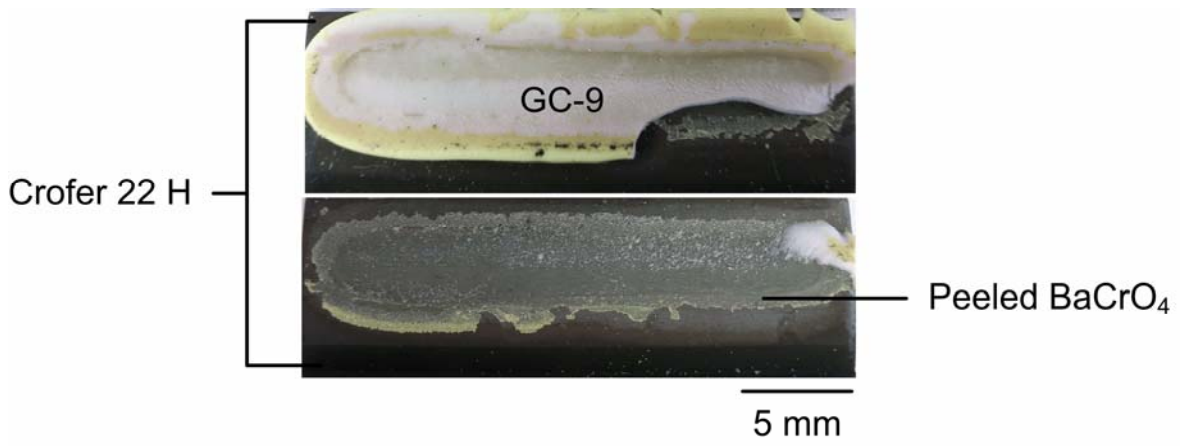


(a)

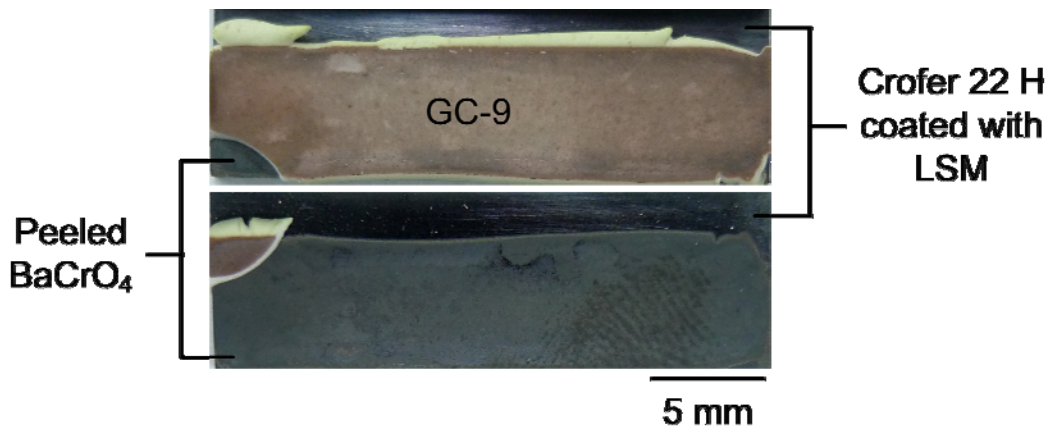


(b)

Fig. 22 Strength of joint specimens with and without LSM coating: (a) shear strength; (b) tensile strength.

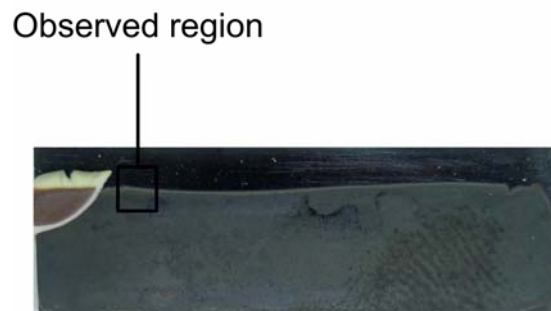


(a)

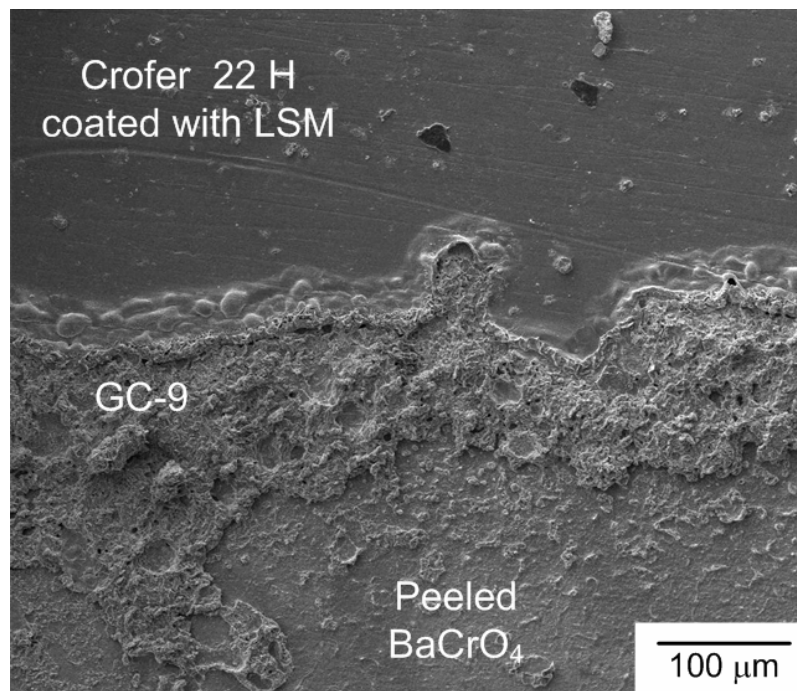


(b)

Fig. 23 Failure patterns of shear specimens tested at 800 °C: (a) HT900 [34] and (b) CHT900.

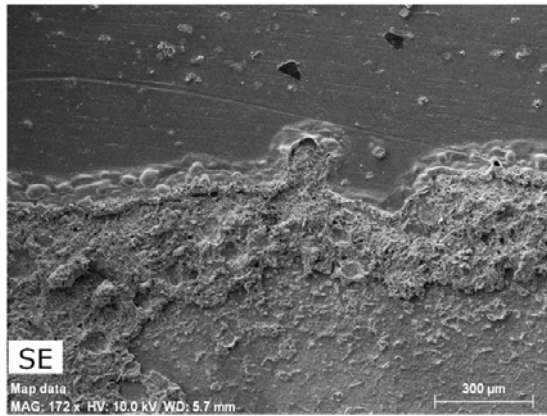


(a)

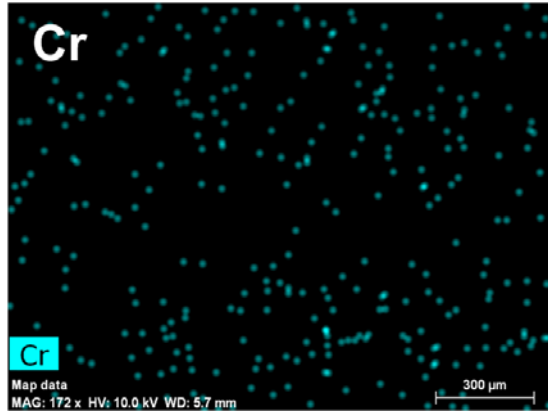


(b)

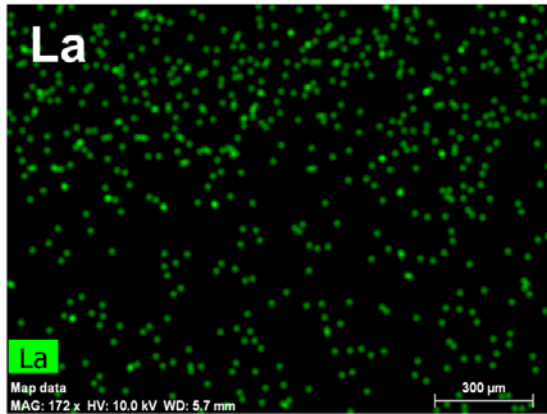
Fig. 24 A fracture surface region without adhered glass-ceramic in a CHT900 specimen: (a) optical micrograph showing the observed region of SEM; (b) SEM micrograph of the outlined region.



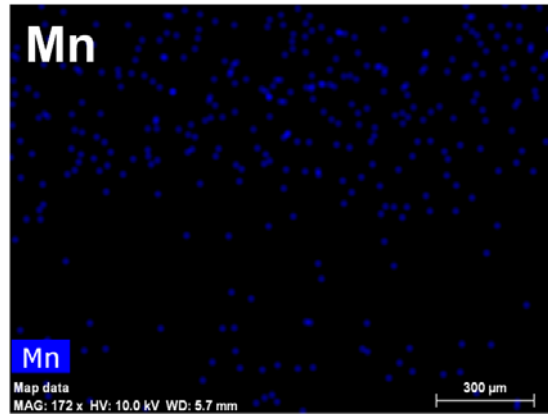
(a)



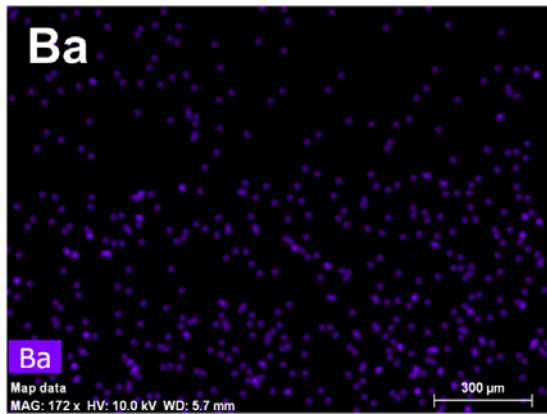
(b)



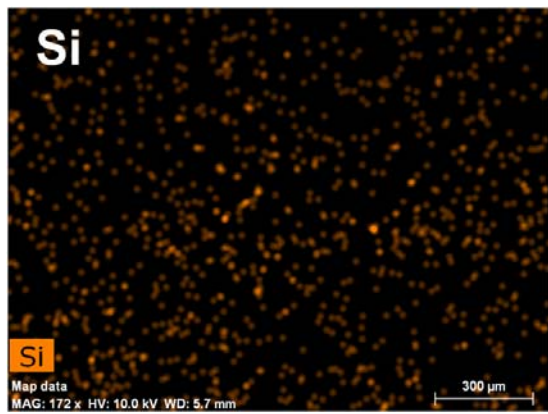
(c)



(d)

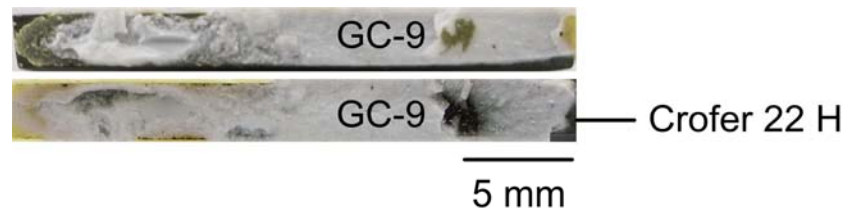


(e)

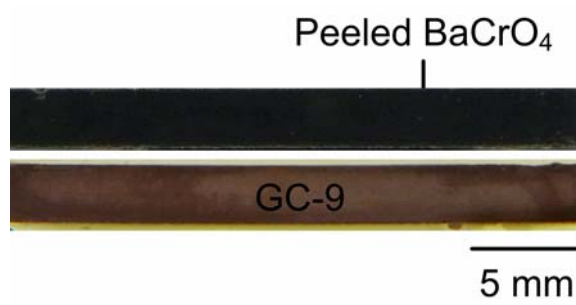


(f)

Fig. 25 EDS mapping of elements on the fracture surface region of a CHT900 specimen outlined in Fig. 24(b) of CHT900: (a) mapping region; (b) Cr; (c) La; (d) Mn; (e) Ba; (f) Si.

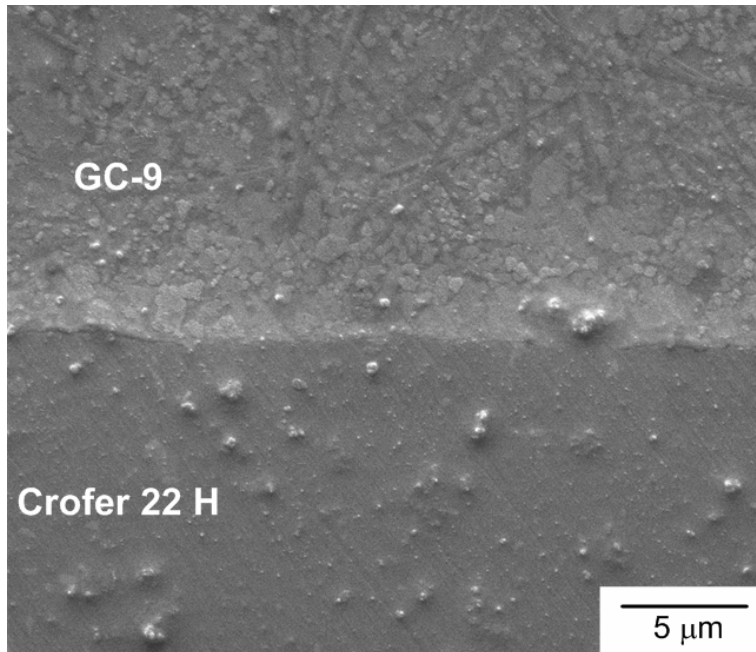


(a)

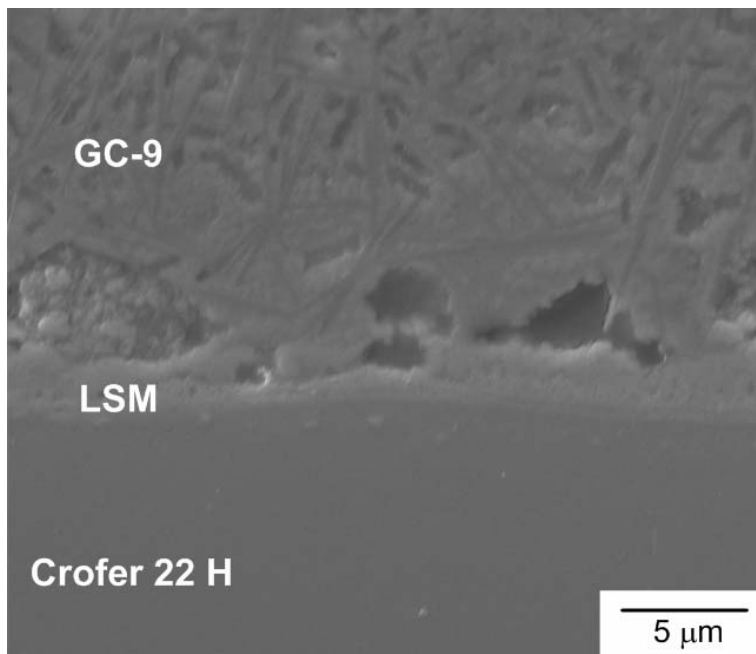


(b)

Fig. 26 Failure patterns of tensile specimens tested at 800 °C: (a) HT900 [34] and (b) CHT900.

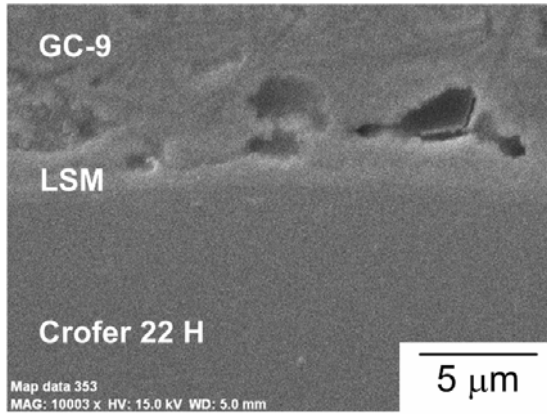


(a)

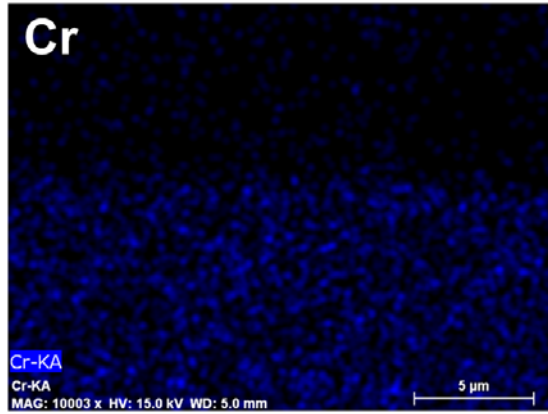


(b)

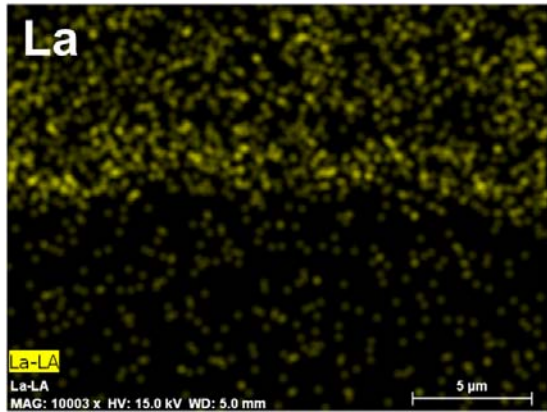
Fig. 27 SEM micrographs of a cross section of the interface between Crofer 22 H and the GC-9 in joint specimens: (a) HT900 [34] and (b) CHT900.



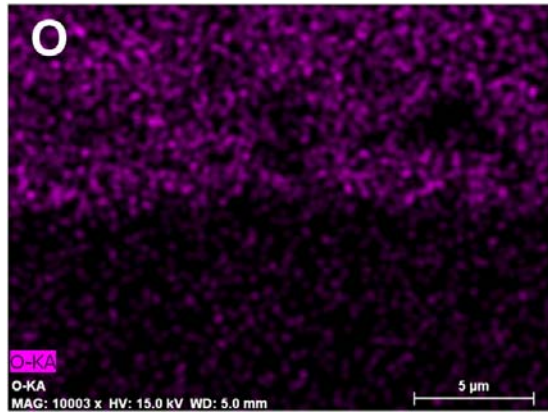
(a)



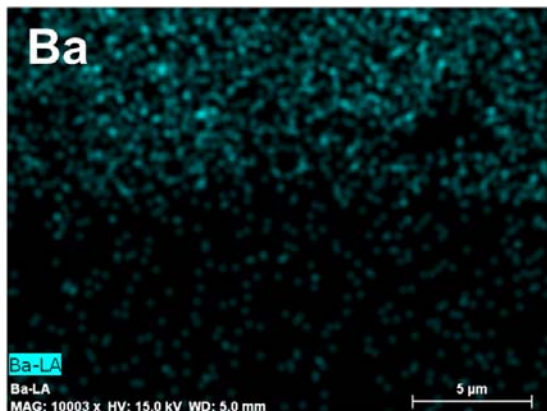
(b)



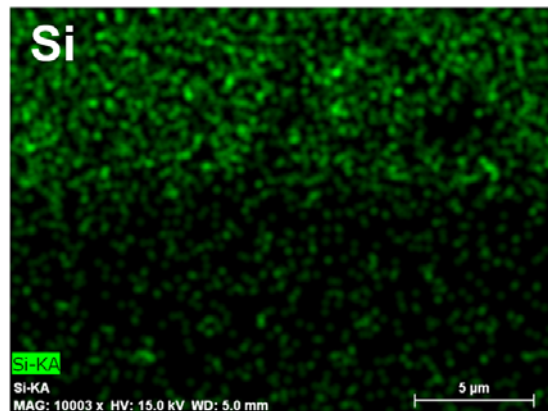
(c)



(d)

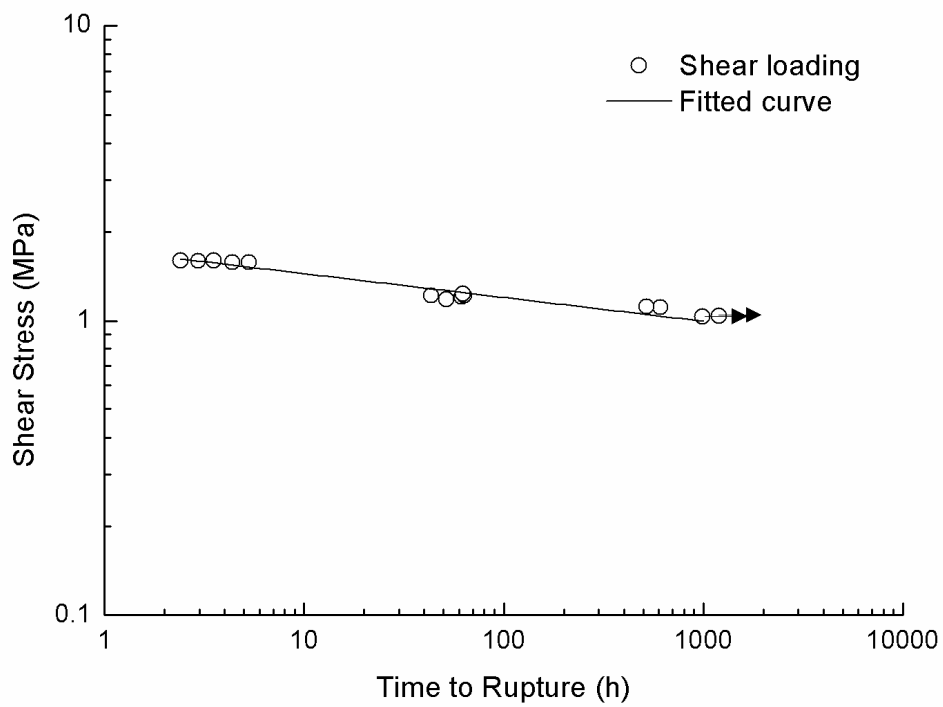


(e)

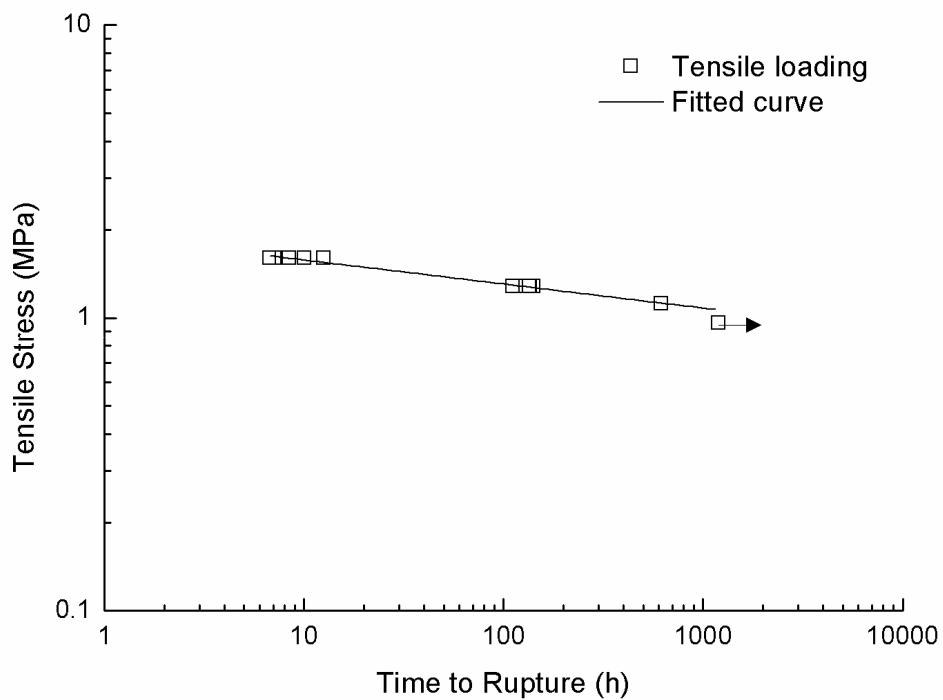


(f)

Fig. 28 EDS mapping of elements at the interface between Crofer 22 H and GC-9 glass in a joint specimen of CHT900: (a) mapping region; (b) Cr; (c) La; (d) O; (e) Ba; (f) Si.



(a)

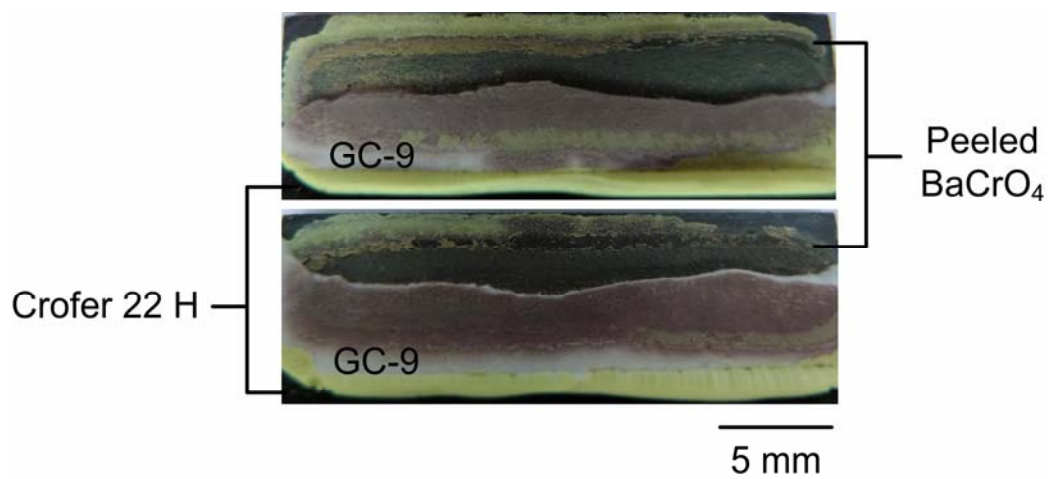


(b)

Fig. 29 Applied stress versus rupture time for the joint specimens subjected to constant (a) shear and (b) tensile loading. (Arrows indicate the specimens were not ruptured when the test was terminated.)

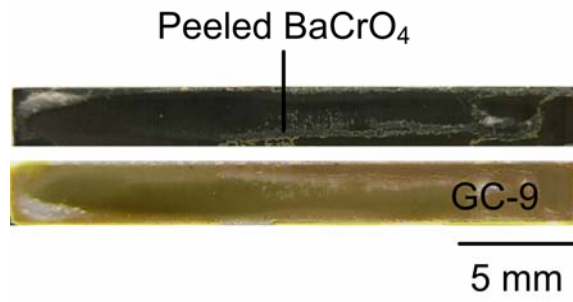


(a)

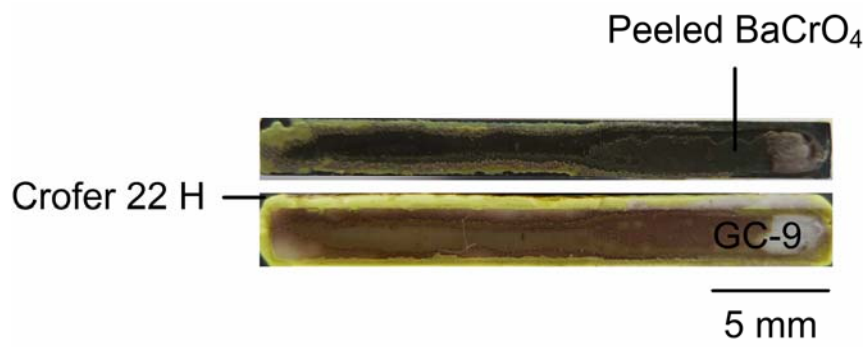


(b)

Fig. 30 Failure patterns in the shear creep specimens tested at 800 °C: (a) shorter creep rupture time and (b) longer creep rupture time.



(a)



(b)

Fig. 31 Failure patterns in the tensile creep specimens tested at 800 °C: (a) shorter creep rupture time and (b) longer creep rupture time.